

# Scatterers on the substrate: Far field formulas

R. Hiptmair and S. Sargheini

Research Report No. 2015-02

January 2015

Latest revision: January 2015

Seminar für Angewandte Mathematik  
Eidgenössische Technische Hochschule  
CH-8092 Zürich  
Switzerland

# Scatterers on substrate: Far field formulas

R. Hiptmair      S. Sargheini

January 19, 2015

## Abstract

The near-field to far-field mapping is a tool used to describe radiation at far distances from scatterers. We consider the geometric setting of a bounded scatterer mounted on a substrate, illuminated by a monochromatic plane wave. For such a structure, the far-field functional consists of different asymptotic terms including surface waves. We investigate all contributions closely and show that the only important term at far distances is the spherical wave. A closed form representation is given based on the Green's function of a dipole over a half space. The far-field functional is stated in terms of both volume and boundary integrals. When finite element methods are used to solve Maxwell's equations approximately, the volume based expression is more accurate than the boundary integral. We confirmed the validity of our results by performing several numerical experiments and compared them with other numerical and experimental results.

## 1 Introduction

In many electromagnetic scattering problems, the key quantity of concern is the radiation pattern at far distances. For example, in antenna measurements the receiver is usually located far away from the sender. Numerical methods such as Finite Elements or Finite Differences provide the solution to Maxwell's equations within some finite region of space, i.e. the field inside the computational domain.

Field values at far distances can be obtained using a post-processing procedure called near-field to far-field mapping. The mapping is a linear functional of the near-field solution. Formulas for far-field calculations for structures in free space is well known. However, for structures located above a substrate, the calculations are more challenging. There have been many investigations about dipole radiation above a half space [16, 4, 6, 11, 10]. Sommerfeld obtained the first formula for a dipole oriented vertically above a planar and lossy plane [20, 19]. The asymptotic evaluation for source and observation points located near the planar surface revealed the contribution of two terms: spherical waves and surface waves [22]. Sommerfeld claimed that surface waves can be used for long distance radio wave transmission due to their slower radial decay along the Earth's surface. However, considering other contributions to the far-field formula shows that surface waves decay exponentially above lossy interfaces. Sommerfeld's results were the basis of many investigations [9, 21, 18].

In this paper we present an asymptotic analysis for outgoing electromagnetic waves and derive a closed form for the field of a dipole over a substrate at far distances. We generalize the dipole results to derive a final form for the near-field to far-field mapping using the Huygens principle. Far-field functionals are stated in terms of a boundary integral over a surface surrounding the scatterer. Since boundary integrals are not well-defined on the natural variational space, we reformulate the far-field mapping in terms of a volume integral. Volume integrals are continuous on the energy space of the variational formulation. As a matter of fact, for Galerkin solutions,

the formulation with the volume-based expression is more appropriate than boundary-integrals for calculating the far-field functional.

To investigate the validity of our results, we analyze the far-field pattern of different structures and compare them with other numerical and experimental results.

## 2 Basics

### 2.1 Potentials

Frequency domain Maxwell's equations for a piecewise constant, linear, homogeneous, isotropic material is

$$\begin{aligned}\nabla \times \mathbf{E}(\mathbf{r}) &= i\omega\mu\mathbf{H}(\mathbf{r}) \\ \nabla \times \mathbf{H}(\mathbf{r}) &= -i\omega\epsilon\mathbf{E}(\mathbf{r}) + \mathbf{J}_i(\mathbf{r}) \\ \nabla \cdot \mu \mathbf{H}(\mathbf{r}) &= 0\end{aligned}\tag{2.1}$$

$$\nabla \cdot \epsilon \mathbf{E}(\mathbf{r}) = -\frac{i}{\omega} \nabla \cdot \mathbf{J}_i(\mathbf{r})$$

where  $\mathbf{E}(\mathbf{r})$  and  $\mathbf{H}(\mathbf{r})$  represent time harmonic electric and magnetic fields at position  $\mathbf{r} \in \mathbb{R}^3$  and angular frequency  $\omega$ .  $\epsilon \in \mathbb{C}$  and  $\mu \in \mathbb{C}$  are permittivity and permeability of the material.  $\mathbf{j}_i(\mathbf{r}, t)$  is the impressed current density. It should be noted that the time dependency  $e^{-i\omega t}$  is considered.

(2.1) consist of two unknown vector fields. In this section we reduce the number of unknowns to one vector and one scalar field by introducing the potentials. The derivation of vector potential is based on the fact that  $\mathbf{B}(\mathbf{r})$  is divergence free. A divergence free field can be expressed as the rotation of a vector field  $\mathbf{A}(\mathbf{r})$

$$\mathbf{H}(\mathbf{r}) = \frac{1}{\mu} \nabla \times \mathbf{A}(\mathbf{r})\tag{2.2}$$

It can also be shown that:

$$\mathbf{E}(\mathbf{r}) = i\omega\mathbf{A}(\mathbf{r}) - \nabla\phi_e(\mathbf{r})\tag{2.3}$$

where  $\phi_e(\mathbf{r}) : \mathbb{R}^3 \rightarrow \mathbb{C}$  is a scalar function.  $\mathbf{A}(\mathbf{r})$  and  $\phi_e(\mathbf{r})$  are known as vector and scalar potentials of an electric source.

To define unique  $\mathbf{A}(\mathbf{r})$  and  $\phi_e(\mathbf{r})$ , we need to put constraints on  $\nabla \cdot \mathbf{A}(\mathbf{r})$ . We can use Lorenz gauge relationship([16], [4]):

$$\nabla \cdot \mathbf{A}(\mathbf{r}) = i\omega\mu\epsilon\phi_e(\mathbf{r})\tag{2.4}$$

Hence, the electric field can be rewritten as:

$$\mathbf{E}(\mathbf{r}) = i\omega \left( \mathbf{A}(\mathbf{r}) + \frac{1}{k^2} \nabla (\nabla \cdot \mathbf{A}(\mathbf{r})) \right)\tag{2.5}$$

where,  $k = \omega\sqrt{\mu\epsilon}$  is the wavenumber.

By coupling equations (2.2) and (2.3), using (2.4), one can derive the vector Helmholtz equation for  $\mathbf{A}(\mathbf{r})$

$$\Delta\mathbf{A}(\mathbf{r}) + k^2\mathbf{A}(\mathbf{r}) = -\mu\mathbf{J}_i(\mathbf{r})\tag{2.6}$$

In Cartesian coordinates, there are three scalar Helmholtz equations embedded in (2.6). One standard technique to solve a second order inhomogeneous partial differential equation such as

scalar Helmholtz equation, is to consider that the source is a point. The solution to the point source is known as Green's function. In the next section, we will study the Green's function for scalar Helmholtz equation.

## 2.2 Green's functions

The Green's function for the scalar Helmholtz equation is obtained by considering a point source at  $\mathbf{r}' = (x', y', z')$

$$\Delta g_0(\mathbf{r}, \mathbf{r}') + k^2 g_0(\mathbf{r}, \mathbf{r}') = \delta(\mathbf{r} - \mathbf{r}'). \quad (2.7)$$

Green's function has to satisfy radiation conditions.

**Proposition 2.1.** (*Sommerfeld radiation condition*) *The solution of (2.7) in unbounded free space must fulfill the radiation condition at infinity*

$$\lim_{r \rightarrow \infty} r \left( \frac{\partial g_0}{\partial r} - ik g_0 \right) = 0. \quad (2.8)$$

where  $r = |\mathbf{r}|$ .

As soon as  $g_0(\mathbf{r}, \mathbf{r}')$  is known, the vector potential can automatically be obtained by an integration over volume  $V$ , where the source term exists

$$\mathbf{A}(\mathbf{r}) = \int_V \mu \mathbf{J}_i(\mathbf{r}') g_0(\mathbf{r}, \mathbf{r}') d\mathbf{r}' \quad (2.9)$$

The solution of the scalar Green's function can also be extended to the electromagnetic field distribution of an electric dipole oriented in direction  $\hat{\ell}$  ( $|\hat{\ell}| = 1$ ). By introducing the vector Green's function  $\mathbf{G}_0(\mathbf{r}, \mathbf{r}', \hat{\ell}) = g_0(\mathbf{r}, \mathbf{r}')\hat{\ell}$  and using (2.2) and (2.5), we have

$$\mathbf{G}^{\mathbf{E}}(\mathbf{r}, \mathbf{r}', \hat{\ell}) = i\omega\mu \left( \mathbf{G}_0(\mathbf{r}, \mathbf{r}', \hat{\ell}) + \frac{1}{k^2} \nabla(\nabla \cdot \mathbf{G}_0(\mathbf{r}, \mathbf{r}', \hat{\ell})) \right) \quad (2.10)$$

$$\mathbf{G}^{\mathbf{H}}(\mathbf{r}, \mathbf{r}', \hat{\ell}) = -\nabla \times \mathbf{G}_0(\mathbf{r}, \mathbf{r}', \hat{\ell})$$

where  $\mathbf{G}^{\mathbf{E}}(\mathbf{r}, \mathbf{r}', \hat{\ell})$  and  $\mathbf{G}^{\mathbf{H}}(\mathbf{r}, \mathbf{r}', \hat{\ell})$  are the electric and magnetic fields observed at  $\mathbf{r} = (x, y, z)$  from an electric dipole located at  $\mathbf{r}' = (x', y', z')$ .

Our main concern in this report is the far-field calculation of structures located either in free space or over a semi-infinite dielectric domain. When computing far-field in Chapter 3, it is shown that it is essential to know  $\mathbf{G}^{\mathbf{E}}(\mathbf{r}, \mathbf{r}', \hat{\ell})$  for the specific geometry. The rest of this chapter is dedicated to the derivation of Green's functions in free space and half space.

### 2.2.1 Dipole in free space

**Theorem 2.1.** *The fundamental solution of (2.7) in free space which has a physical interpretation is [4, Sec. 1.3.4],*

$$g_0(\mathbf{r}, \mathbf{r}') = \frac{\exp(\pm ik|\mathbf{r} - \mathbf{r}'|)}{4\pi|\mathbf{r} - \mathbf{r}'|}. \quad (2.11)$$

Obviously,  $g_0(\mathbf{r}, \mathbf{r}')$  satisfies the radiation condition (2.8).

The spatial Fourier transformation of (2.11) can be obtained by the Weyl identity [21]

$$g_0(\mathbf{r}, \mathbf{r}') = \frac{i}{8\pi^2} \int_{-\infty}^{+\infty} \int_{-\infty}^{+\infty} \frac{\exp(i(k_x(x-x') + k_y(y-y') + k_z(k_x, k_y)|z-z'|))}{k_z(k_x, k_y)} dk_x dk_y \quad (2.12)$$

where  $\mathbf{k} = (k_x, k_y, k_z)$  is the wave vector. (2.12) is obtained using the method of separation of variables, and  $|\mathbf{k}| = k$ , so  $k_z(k_x, k_y) = \sqrt{k^2 - (k_x^2 + k_y^2)}$ . The square root makes  $k_z$  a double valued number. The Standard square root branch cut along negative real axis is used to treat the double valued numbers (see Section 2.3).

In Cartesian coordinates, plane waves  $e^{i\mathbf{k}\cdot\mathbf{r}}$  are the solution of the homogeneous Helmholtz equation. This solution is also obtained using the separation of variables. As a matter of fact, (2.12) is usually called the plane-wave expansion of function  $g_0(\mathbf{r}, \mathbf{r}')$ .

To reduce the number of integrals in (2.12), one can use cylindrical waves instead of plane waves. The cylindrical wave expansion of (2.11) is called the Sommerfeld identity [20, Page 242]

$$g_0(\mathbf{r}, \mathbf{r}') = \frac{i}{4\pi} \int_0^{+\infty} k_\rho J_0(k_\rho \bar{\rho}) \frac{\exp(ik_z(k_\rho) |z - z'|)}{k_z(k_\rho)} dk_\rho. \quad (2.13)$$

where  $\bar{\rho} = |(x, y) - (x', y')|$ ,  $k_z(k_\rho) = \sqrt{k^2 - k_\rho^2}$ , and  $J_0(k_\rho \bar{\rho})$  is the zero order Bessel function of the first kind. Similar to (2.12),  $k_z(k_\rho)$  is double valued and is the source of branch points at  $k_\rho = \pm k$  (see Section 2.3).

For subsequent applications, it is more useful to have the integration range from  $-\infty$  to  $+\infty$  in (2.13). For this end, we put

$$J_0(k_\rho \bar{\rho}) = \frac{1}{2} (H_0^1(k_\rho \bar{\rho}) + H_0^2(k_\rho \bar{\rho})) \quad (2.14)$$

Using the change of variables  $\hat{k}_\rho = -k_\rho$  and keeping in mind that  $H_0^2(-k_\rho \bar{\rho}) = -H_0^1(k_\rho \bar{\rho})$ , we have

$$\begin{aligned} \int_0^{+\infty} k_\rho H_0^2(k_\rho \bar{\rho}) \frac{\exp(ik_z(k_\rho) |z - z'|)}{k_z(k_\rho)} dk_\rho = \\ \int_{-\infty}^0 \hat{k}_\rho H_0^1(\hat{k}_\rho \bar{\rho}) \frac{\exp(ik_z(\hat{k}_\rho) |z - z'|)}{k_z(\hat{k}_\rho)} d\hat{k}_\rho \end{aligned} \quad (2.15)$$

**Remark 2.1.** *If the range of  $k_\rho$  in (2.13) is to be extended to  $k_\rho = -\infty$ , one must take into account that a branch point singularity at  $k_\rho = 0$  arises from the Bessel function. To preserve the integrand single valued in the complex  $k_\rho$  plane, we introduce a branch cut along the negative real  $k_\rho$  axis (see Figure 1).*

Finally, we obtain

$$g_0(\mathbf{r}, \mathbf{r}') = \frac{i}{8\pi} \int_{\bar{P}_\rho} \hat{k}_\rho H_0^1(\hat{k}_\rho \bar{\rho}) \frac{\exp(ik_z(\hat{k}_\rho) |z - z'|)}{k_z(\hat{k}_\rho)} d\hat{k}_\rho. \quad (2.16)$$

where  $H_0^1(\hat{k}_\rho \bar{\rho})$  and  $H_0^2(\hat{k}_\rho \bar{\rho})$  are zero order Hankel functions of the first and the second kind, respectively.  $\bar{P}_\rho$  is the integration contour in complex  $k_\rho$  plane as depicted in Figure 1.

The integrals in (2.12) and (2.16) are improper. They will converge only if  $\exp(ik_z |z - z'|)$  converges to zero as the integration parameters approach  $+\infty$  or  $-\infty$ . To fulfill this condition, it is necessary to impose  $\text{Im } k_z > 0$ . In Section 2.3, it is thoroughly discussed how the selection of branch cuts helps us to keep the imaginary part of  $k_z$  always positive along the integration contour.

The branch cuts in (2.16) can be removed by introducing the complex angle  $w$ :

$$k_\rho = k \sin w \quad (2.17)$$

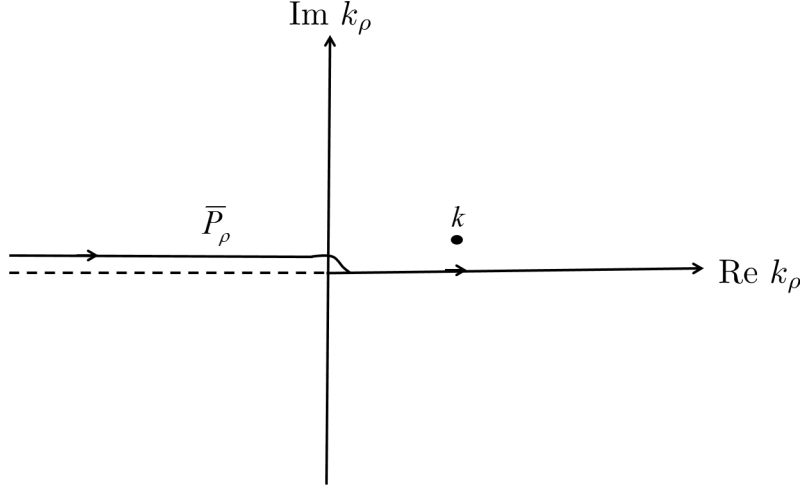


Figure 1: Integration contour in the complex  $k_\rho$  plane.

In Section 2.3 it is shown that  $k_z(k_\rho)$  is no more double valued in complex  $w$  plane

$$k_z(w) = +k \cos w \quad (2.18)$$

(2.16) in terms of  $w$  is

$$g_0(\mathbf{r}, \mathbf{r}') = \frac{i k}{8\pi} \int_{\bar{P}_w} \sin w H_0^1(k\bar{\rho} \sin w) e^{(ik_z(w)|z-z'|)} dw \quad (2.19)$$

where  $\bar{P}_w$  is the transformed integration path in the  $w$  plane.

For real values of  $k$  we obtain from (2.17)

$$k_\rho = k(\sin(\text{Re } w) \cosh(\text{Im } w) + i \cos(\text{Re } w) \sinh(\text{Im } w)) \quad (2.20)$$

Thus,  $\bar{P}_w$  lies on

$$\text{Im } k_\rho = k \cos(\text{Re } w) \sinh(\text{Im } w) = 0 \quad (2.21)$$

This implies that

$$\begin{cases} \text{If } \text{Im } w = 0 \text{ then } \text{Im } k_\rho = 0 \ \& \ -k \leq \text{Re } k_\rho \leq k \\ \text{If } \text{Re } w = \frac{\pi}{2} \text{ then } \text{Im } k_\rho = 0 \ \& \ \text{Re } k_\rho \geq k \\ \text{If } \text{Re } w = \frac{-\pi}{2} \text{ then } \text{Im } k_\rho = 0 \ \& \ \text{Re } k_\rho \leq -k \end{cases} \quad (2.22)$$

Similar to (2.12) and (2.16), the integral in (2.19) is improper. Consequently, the direction of  $\bar{P}_w$  must be chosen in such a way that  $\text{Im } k_z(w) > 0$ . Using (2.18), one can simply show that  $\text{Im } k_z = -k \sin(\text{Re } w) \sinh(\text{Im } w)$  for real values of  $k$ . In order to keep the imaginary part of  $k_z$  always positive along  $\bar{P}_w$  we must have the followings

- If  $\text{Re } w = \frac{\pi}{2}$   
the contour folds down towards  $\text{Im } w < 0$ .
- If  $\text{Re } w = \frac{-\pi}{2}$   
the contour folds up towards  $\text{Im } w > 0$

The final form of  $\bar{P}_w$  is shown in Figure 2.

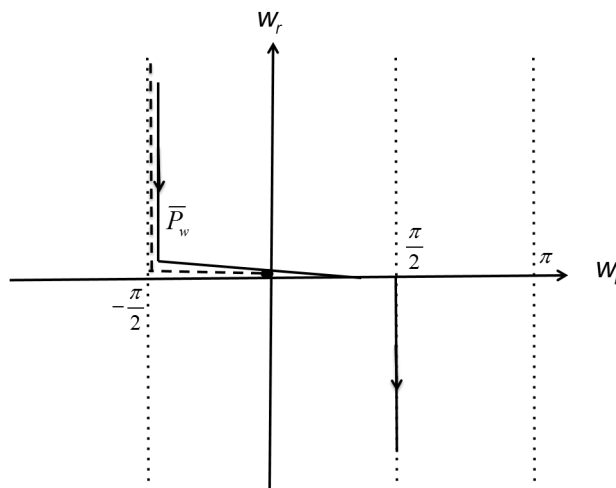


Figure 2: Integration contour in the complex  $w$  plane.

### 2.2.2 Dipole over a semi-infinite surface

Figure 3 shows a dipole located over a semi-infinite domain (substrate).  $\Omega_1 := \{\mathbf{r} \in \mathbb{R}^3 : z > 0\}$  and  $\Omega_2 := \{\mathbf{r} \in \mathbb{R}^3 : z < 0\}$ .  $(\epsilon_1, \mu_1)$  and  $(\epsilon_2, \mu_2)$  are the material properties of  $\Omega_1$  and  $\Omega_2$ , respectively.

**Assumption 1.** *In this report, we consider non magnetic ( $\mu_\alpha =$  permeability of free space  $\mu_0$ ), loss-free ( $\text{Im } \epsilon_\alpha = 0$ ) or lossy ( $\text{Im } \epsilon_\alpha > 0$ ) dielectrics. For the sake of simplicity we assume  $\text{Re } \epsilon_\alpha \geq 0$ .  $\alpha = 1, 2$  specifies different coefficients for different subdomains  $\Omega_\alpha$*

Wavenumbers in  $\Omega_1$  and  $\Omega_2$  are  $k_1 = n_1 k_0$  and  $k_2 = n_2 k_0$ , respectively. Note that  $k_0 = \omega \sqrt{\epsilon_0 \mu_0}$  is the wavenumber in free space, and  $n_1 = \sqrt{\frac{\epsilon_1}{\epsilon_0}}$  and  $n_2 = \sqrt{\frac{\epsilon_2}{\epsilon_0}}$  are refraction indices.

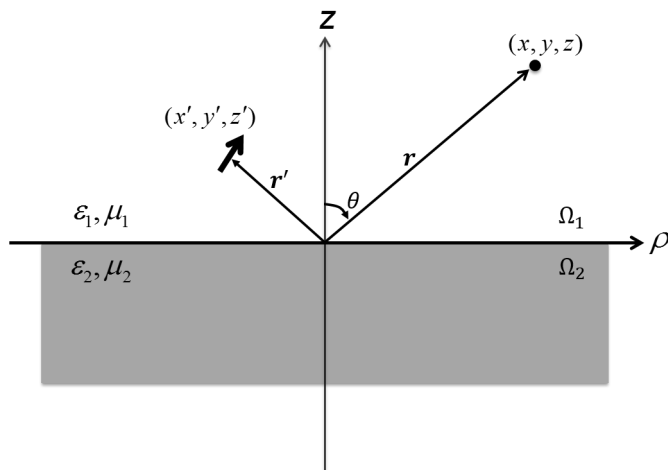


Figure 3: Dipole located over a semi-infinite dielectric domain.

The best way to find the solution of (2.7) in the presence of a substrate is to start with the solution in free space. As already mentioned, the integrand in (2.12) is a linear superposition of plane waves. Plane waves in the presence of a semi-infinite dielectric domain can be decomposed into transverse electric (TE) and transverse magnetic (TM) modes [4, Ch.2]. The electric field of a TE mode is perpendicular to the plane of incidence, whereas, the magnetic field of a TM mode is perpendicular to the plane of incidence. The plane of incidence is a plane spanned by vectors  $\mathbf{k}$  and  $\hat{n}$ , where  $\hat{n}$  is the unit vector normal to the substrate. In the configuration shown in Figure 3 we have  $\hat{n} = \hat{z}$ .

A TM wave incidence on a half space is depicted in Figure 4. The  $z$  component of the incident electric field is  $E_z^i = E_0 e^{i(k_x x + k_y y - k_{z_1} z)}$ .  $\mathbf{k}_1 = (k_x, k_y, k_{z_1})$  and  $\mathbf{k}_2 = (k_x, k_y, k_{z_2})$  both belong to  $\mathbb{R}^3$  in a way that  $|\mathbf{k}_1| = k_1$  and  $|\mathbf{k}_2| = k_2$ .

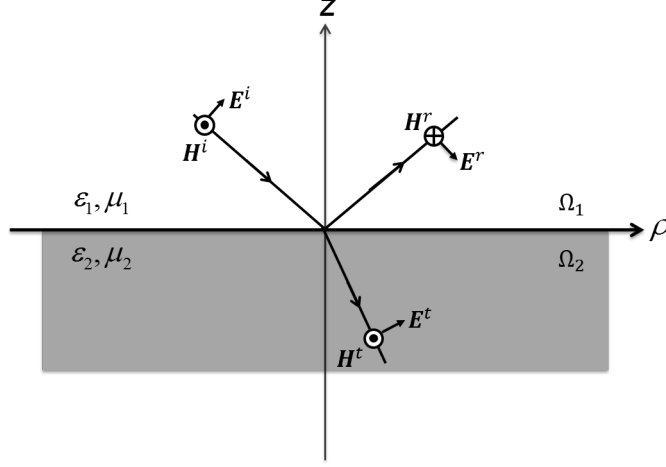


Figure 4: TM wave incidence on a semi-infinite dielectric half space.  $(\mathbf{E}^i(\mathbf{r}), \mathbf{H}^i(\mathbf{r}))$ ,  $(\mathbf{E}^r(\mathbf{r}), \mathbf{H}^r(\mathbf{r}))$ , and  $(\mathbf{E}^t(\mathbf{r}), \mathbf{H}^t(\mathbf{r}))$  are the incident, reflected, and transmitted fields, respectively.

**Proposition 2.2.** ([16, Sec. 2.8.1]) Consider an incident TM wave over a semi-infinite half space shown in Figure 3 with  $E_z^i = E_0 e^{i(k_x x + k_y y - k_{z_1} z)}$ . Then the longitudinal component of the total field is

$$TM : \begin{cases} E_z(\mathbf{r}) = E_0 e^{i(k_x x + k_y y - k_{z_1} z)} \\ \quad - R^{TM}(k_x, k_y) E_0 e^{i(k_x x + k_y y + k_{z_1} z)} & \text{in } \Omega_1 \\ E_z(\mathbf{r}) = T^{TM}(k_x, k_y) E_0 e^{i(k_x x + k_y y - k_{z_2} z)} & \text{in } \Omega_2 \\ H_z(\mathbf{r}) = 0 & \text{in } \Omega_1 \text{ \& \not\in } \Omega_2 \end{cases} \quad (2.23)$$

where  $R^{TM}(k_x, k_y)$  and  $T^{TM}(k_x, k_y)$  are reflection and transmission coefficients of TM modes, respectively

$$\begin{aligned} R^{TM}(k_x, k_y) &= \frac{\epsilon_1 k_{z_2} - \epsilon_2 k_{z_1}}{\epsilon_1 k_{z_2} + \epsilon_2 k_{z_1}} \\ T^{TM}(k_x, k_y) &= 1 + R^{TM}(k_x, k_y) \end{aligned} \quad (2.24)$$

**Proposition 2.3.** ([16, Sec. 2.8.1], Consider an incident TE wave over a semi-infinite half space shown in Figure 3 with  $H_z^i = H_0 e^{i(k_x x + k_y y - k_{z_1} z)}$ . Then the longitudinal component of the total field is

$$TE : \begin{cases} E_z(\mathbf{r}) = 0 & \text{in } \Omega_1 \text{ \& \not\in } \Omega_2 \\ H_z(\mathbf{r}) = H_0 e^{i(k_x x + k_y y - k_{z_1} z)} \\ \quad + R^{TE}(k_x, k_y) H_0 e^{i(k_x x + k_y y + k_{z_1} z)} & \text{in } \Omega_1 \\ H_z(\mathbf{r}) = T^{TE}(k_x, k_y) H_0 e^{i(k_x x - k_y y - k_{z_2} z)} & \text{in } \Omega_2 \end{cases} \quad (2.25)$$

with reflection and transmission coefficients  $R^{TE}$  and  $T^{TE}$ :

$$\begin{aligned} R^{TE}(k_x, k_y) &= \frac{k_{z_1} - k_{z_2}}{k_{z_1} + k_{z_2}} \\ T^{TE}(k_x, k_y) &= 1 + R^{TE}(k_x, k_y) \end{aligned} \quad (2.26)$$

Note that  $k_{z_1}(k_x, k_y) = \sqrt{k_1^2 - k_x^2 - k_y^2}$  and  $k_{z_2}(k_x, k_y) = \sqrt{k_2^2 - k_x^2 - k_y^2}$  both are double valued functions and must be treated using branch cuts (see Section 2.3).

In order to expand the field of a dipole oriented in direction  $\hat{\ell}$  above a substrate using plane waves, one must choose the correct mode of plane waves. Based on what discussed already the longitudinal component of the electric field of a dipole  $\mathbf{G}^{\mathbf{E}}(\mathbf{r}, \mathbf{r}', \hat{\ell}) \cdot \hat{z}$  must be expanded using TM waves, and similarly the longitudinal component of the magnetic field of a dipole  $\mathbf{G}^{\mathbf{H}}(\mathbf{r}, \mathbf{r}', \hat{\ell}) \cdot \hat{z}$  must be expanded in terms of TE waves.

Using (2.12), one can derive the plane wave expansion of the scalar Green's function in the presence of a planar dielectric half space in terms of either TM or TE mode expansion

$$g_0(\mathbf{r}, \mathbf{r}') = \begin{cases} \frac{i}{8\pi} \int_{-\infty}^{+\infty} \int_{-\infty}^{+\infty} \frac{e^{i(k_x(x-x') + k_y(y-y') + k_{z_1}(k_x, k_y)z)}}{k_{z_1}(k_x, k_y)} & \mathbf{r} \in \Omega_1 \\ \left[ e^{-ik_{z_1}(k_x, k_y)z'} + f(k_x, k_y)e^{ik_{z_1}(k_x, k_y)z'} \right] dk_x dk_y & \\ \\ \frac{i}{8\pi} \int_{-\infty}^{+\infty} \int_{-\infty}^{+\infty} \frac{e^{i(k_x(x-x') + k_y(y-y') - k_{z_2}(k_x, k_y)z + k_{z_1}(k_x, k_y)z')}}{k_{z_1}(k_x, k_y)} & \mathbf{r} \in \Omega_2 \\ (1 + f(k_x, k_y)) dk_x dk_y & \end{cases} \quad (2.27)$$

where  $f(k_x, k_y) = -R^{TM}(k_x, k_y)$  for TM modes, and  $f(k_x, k_y) = R^{TE}(k_x, k_y)$  for TE modes.

**Assumption 2.** Green's functions derived in this report are for  $\mathbf{r}' \in \Omega_1$ . A similar procedure can be used to calculate  $g_0(\mathbf{r}, \mathbf{r}')$  for  $\mathbf{r}' \in \Omega_2$

In terms of cylindrical waves (2.27) is

$$g_0(\mathbf{r}, \mathbf{r}') = \begin{cases} \frac{i}{8\pi} \int_{\bar{P}_\rho} \frac{k_\rho H_0^1(k_\rho \bar{\rho})}{k_{z_1}(k_\rho)} e^{ik_{z_1}(k_\rho)z} & \mathbf{r} \in \Omega_1 \\ \left[ e^{-ik_{z_1}(k_\rho)z'} + f(k_\rho)e^{ik_{z_1}(k_\rho)z'} \right] dk_\rho & \\ \\ \frac{i}{8\pi} \int_{\bar{P}_\rho} \frac{k_\rho H_0^1(k_\rho \bar{\rho})}{k_{z_1}(k_\rho)} e^{i(k_{z_1}(k_\rho)z' - k_{z_2}(k_\rho)z)} (1 + f(k_\rho)) dk_\rho & \mathbf{r} \in \Omega_2 \end{cases} \quad (2.28)$$

where  $\bar{\rho} = |(x, y) - (x', y')|$ ,  $k_{z_1}(k_\rho) = \sqrt{k_1^2 - k_\rho^2}$  and  $k_{z_2}(k_\rho) = \sqrt{k_2^2 - k_\rho^2}$ . Double valued functions  $k_{z_1}(k_\rho)$  and  $k_{z_2}(k_\rho)$  are the sources of branch cuts at  $k_\rho = \pm k_1$  and  $k_\rho = \pm k_2$  in both half spaces (see Section 2.3).  $f(k_\rho)$  is derived in a similar way to  $f(k_x, k_y)$  just by considering  $k_{z_1}(k_\rho)$  and  $k_{z_2}(k_\rho)$  instead of  $k_{z_1}(k_x, k_y)$  and  $k_{z_2}(k_x, k_y)$ , respectively.

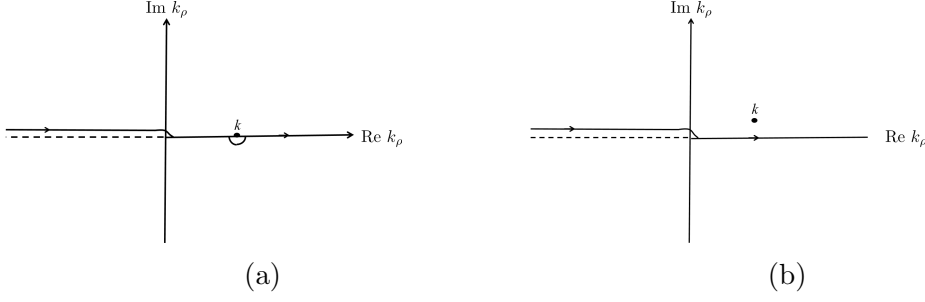


Figure 5: Integration path in the complex  $k_\rho$  plane for a (a) loss-less (b) lossy material.

In terms of the complex angle  $w$ , (2.28) is

$$g_0(\mathbf{r}, \mathbf{r}') = \begin{cases} \frac{i k_1}{8\pi} \int_{\bar{P}_w} \sin w H_0^1(k_1 \bar{\rho} \sin w) e^{(ik_{z_1}(w) z)} \\ \quad \left[ e^{(-ik_{z_1}(w) z')} + f(w) e^{(ik_{z_1}(w) z')} \right] dw & \mathbf{r} \in \Omega_1 \\ \frac{i k_2}{8\pi} \int_{\bar{P}_w} \sin w H_0^1(k_2 \bar{\rho} \sin w) e^{(-ik_{z_2}(w) z)} \\ \quad e^{(ik_{z_1}(w) z')} (1 + f(w)) dw & \mathbf{r} \in \Omega_2 \end{cases} \quad (2.29)$$

where

$$\begin{cases} k_{z_1}(w) = +k_1 \cos w \\ k_{z_2}(w) = k_1 \sqrt{\frac{\epsilon_2}{\epsilon_1} - \sin^2 w} \end{cases} \quad \text{in } \Omega_1 \quad (2.30)$$

$$\begin{cases} k_{z_1}(w) = k_2 \sqrt{\frac{\epsilon_1}{\epsilon_2} - \sin^2 w} \\ k_{z_2}(w) = -k_2 \cos w \end{cases} \quad \text{in } \Omega_2. \quad (2.31)$$

$k_{z_2}(w)$  and  $k_{z_1}(w)$  are the sources of branch cuts in  $\Omega_1$  and  $\Omega_2$ , respectively (see Section 2.3).  $f(w)$  is derived in a similar way to  $f(k_x, k_y)$  just by considering  $k_{z_1}(w)$  and  $k_{z_2}(w)$  instead of  $k_{z_1}(k_x, k_y)$  and  $k_{z_2}(k_x, k_y)$ , respectively.

## 2.3 Branch cuts

The integrand in (2.28) contains branch point singularities at  $k_\rho = \pm k_1$  and  $k_\rho = \pm k_2$  which arise from  $k_{z_1} = \sqrt{k_1^2 - k_\rho^2}$  and  $k_{z_2} = \sqrt{k_2^2 - k_\rho^2}$ , respectively [1]. In loss-less materials, the branch points lie on the integration path. Then the integration path must be displaced around singularities (see Figure 5a). By introducing a slight loss in materials,  $k_1$  and  $k_2$  have small positive imaginary parts, thus the branch points are no more on the real axis. Typical Integration paths in complex  $k_\rho$  plane for loss-less and lossy materials are shown in Figure 5a and 5b, respectively.

Branch cuts originating from double valued functions in a complex plane, e.g.  $k_{z_1}$  and  $k_{z_2}$ , provide a mean to pass from one Riemann sheet to the other [1]. Signs of  $\text{Im } k_{z_1}$ , and  $\text{Im } k_{z_2}$  in different regions of  $k_\rho$  plane depend on Riemann sheet junctions or branch cuts. To ensure the boundedness of integrands in (2.28) when  $k_{z_1}|z - z'| \rightarrow \infty$  or  $k_{z_2}|z - z'| \rightarrow \infty$ , it is necessary to

impose conditions  $\text{Im } k_{z_1} > 0$  and  $\text{Im } k_{z_2} > 0$ . As a matter of fact, the boundedness of radiation integrals is closely related to branch cuts.

The selection of branch cuts is arbitrary, but cuts along contours  $\text{Im } k_{z_\alpha} = 0$  or  $\text{Re } k_{z_\alpha} = 0$ ,  $\alpha = 1, 2$  are very useful. If one chooses branch cuts along  $\text{Im } k_{z_\alpha} = 0$ , then  $\text{Im } k_{z_\alpha} > 0$  in the whole top Riemann sheet, and the sign of  $\text{Re } k_{z_\alpha}$  changes when  $k_\rho$  crosses the cuts. In [6, Sec. 5.3b], it has been thoroughly argued that  $\text{Im } k_{z_\alpha} = 0$  and  $\text{Re } k_{z_\alpha} = 0$  are along the hyperbola  $\text{Re } k_\rho \text{Im } k_\rho = \text{Re } k_\alpha \text{Im } k_\alpha$  for  $|\text{Re } k_\rho| < \text{Re } k_\alpha$  and  $|\text{Re } k_\rho| > \text{Re } k_\alpha$ , respectively (see Figure 6).

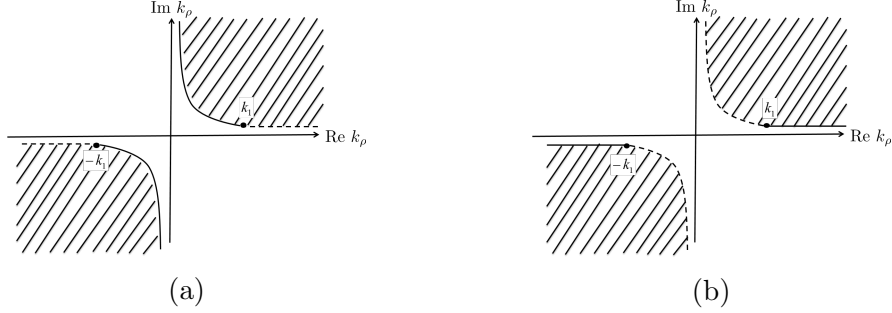


Figure 6: Different choices of branch cuts in the complex  $k_\rho$  plane. (a) Branch cuts are along  $\text{Im } k_z = 0$ . So,  $\text{Im } k_z > 0$  on the entire top Riemann sheet,  $\text{Re } k_z > 0$  on shaded regions,  $\text{Re } k_z < 0$  on unshaded regions. (b) Branch cuts are along  $\text{Re } k_z = 0$ . So,  $\text{Im } k_z > 0$  on the entire top Riemann sheet,  $\text{Im } k_z > 0$  on shaded regions,  $\text{Im } k_z < 0$  on unshaded regions.

The number of branch cuts can be reduced to one, if we use the change of variables (2.17). To discuss this more clearly, we focus on the first integration in (2.29). A similar procedure can be applied for the radiation integral in  $\Omega_2$ .

The transformation (2.17) is  $2\pi$  periodic with respect to  $\text{Re } w$ . Thus, the entire  $k_\rho$  plane can be mapped into various adjacent sections of width  $2\pi$  in the  $w$  plane. For the sake of simplicity, we only consider the interval  $-\pi < \text{Re } w < \pi$ .

For a loss-less material, (2.30) boils down to

$$\text{Im } k_{z_1} = -k_1 \sin(\text{Re } w) \sinh(\text{Im } w) \quad (2.32)$$

It is easy to see that  $\text{Im } k_{z_1} > 0$  for  $\begin{cases} -\pi < \text{Re } w < 0 & \text{and } \text{Im } w > 0 \\ 0 < \text{Re } w < \pi & \text{and } \text{Im } w < 0 \end{cases}$

As a matter of fact, (2.17) maps the two-sheeted  $k_\rho$  plane (with respect to  $k_{z_1}$ ) into adjacent regions in the  $w$  plane, that is  $k_{z_1} = \sqrt{k_1^2 - k_\rho^2} = 0$  is no more double valued and no branch cut arises from it. However,  $k_{z_2} = k_1 \sqrt{\eta - \sin^2 w}$  is still a source of a branch cut which originates from the branch point  $\sin w_b = \sqrt{\eta}$ . Note that  $\eta = \frac{\epsilon_2}{\epsilon_1}$ .

### 3 Far-field calculations

**Theorem 3.1.** ([4, Sec. 1.4], Huygens' principle) *Let  $D$  be a finite domain which contains all the electromagnetic sources. Furthermore, consider a closed surface  $\Gamma$  which surrounds  $D$  (see Figure 7). Then the scattered field distribution on  $\Gamma$  can be extended to the scattered field*

outside the surface  $\Gamma$

$$\mathbf{E}(\mathbf{r}) \cdot \hat{\ell} = \frac{1}{i\omega\mu} \int_{\Gamma} (\nabla^{\mathbf{r}'} \times \mathbf{E}(\mathbf{r}')) \cdot \left( \mathbf{G}^{\mathbf{E}}(\mathbf{r}, \mathbf{r}', \hat{\ell}) \times \hat{n}(\mathbf{r}') \right) + \left( \nabla^{\mathbf{r}} \times \mathbf{G}^{\mathbf{E}}(\mathbf{r}, \mathbf{r}', \hat{\ell}) \right) \cdot (\mathbf{E}(\mathbf{r}') \times \hat{n}(\mathbf{r}')) ds(\mathbf{r}') \quad (3.1)$$

where  $\nabla^{\mathbf{r}}$  and  $\nabla^{\mathbf{r}'}$  are derivatives with respect to parameter  $\mathbf{r}$  and  $\mathbf{r}'$ , respectively, and  $\hat{n}$  is the outward-pointing normal vector on  $\Gamma$ .  $\mathbf{G}^{\mathbf{E}}(\mathbf{r}, \mathbf{r}', \hat{\ell})$  is the electric field of an electric dipole, oriented in direction  $\hat{\ell}$  and located at  $\mathbf{r}'$ , observed at point  $\mathbf{r}$ .

(3.1) is also known as representation formula [15, Ch. 3, Thm. 3.1.1].

In the case of a scattering problem  $D$  is the scatterer which contains all sources of the scattered field.

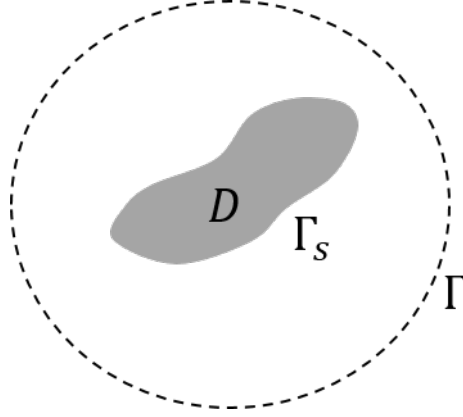


Figure 7: The scatterer  $D$  is shown as a shaded region bounded by  $\Gamma_S$ . The Integral in (3.1) is calculated over the contour  $\Gamma$

Equation (3.1) can be simplified when the observation point is located far away from the scatterer, i.e.  $kr \rightarrow \infty$ . Since (3.1) relies basically on the electric field distribution of an electric dipole  $\mathbf{G}^{\mathbf{E}}(\mathbf{r}, \mathbf{r}', \hat{\ell})$ , the primary emphasis is on investigating the far-field behavior of a single dipole in free space and in semi-infinite half space. The Green's function for free space is implicitly embedded inside the formulation for the half space. Henceforth, we mainly discuss the half-space problem. Among three forms of the scalar Green's function represented in (2.27), (2.28), and (2.29), we use (2.29), since it has a reduced number of branch cuts.

To study the behavior of (2.29) at far distances, one needs to evaluate it asymptotically. To put (2.29) in a proper form for the asymptotic analysis, we do one more step of simplification and employ the large-argument approximation of Hankel function for far-field observation points

$$H_n^1(z) = \sqrt{\frac{2}{\pi z}} \left( e^{i(z - \frac{n\pi}{2} - \frac{\pi}{4})} + O\left(\frac{1}{z}\right) \right) \text{ for } |z| \gg n \quad |\arg z| < \pi. \quad (3.2)$$

One can also show that

$$\bar{\rho} \sim \rho - \rho' \cos(\phi - \phi') \quad \text{as } \rho \rightarrow \infty \quad (3.3)$$

where  $\rho = |(x, y)|$ ,  $\rho' = |(x', y')|$ ,  $(x, y) = \rho(\cos \phi, \sin \phi)$ , and  $(x', y') = \rho'(\cos \phi', \sin \phi')$ .

**Remark 3.1.** If the function  $f(x)$  is asymptotically equivalent to  $g(x)$  under the limit  $x \rightarrow x_0$ , that is  $\lim_{x \rightarrow x_0} \frac{f(x)}{g(x)} = 1$ , we write [14, Pgae 4]

$$f(x) \sim g(x) \text{ as } x \rightarrow x_0. \quad (3.4)$$

Using (3.4) and (3.3), we rewrite (2.29) as

$$g_0(\mathbf{r}, \mathbf{r}') \sim C(\mathbf{r}, \mathbf{r}') \int_{\bar{P}_w} \mathcal{V}(w, \mathbf{r}, \mathbf{r}') e^{r\psi(w, \mathbf{r}, \mathbf{r}')} dw \text{ as } r \rightarrow \infty \quad (3.5)$$

where  $C(\mathbf{r}, \mathbf{r}') = \frac{e^{i\frac{\pi}{4}}}{8\pi} \sqrt{\frac{2k_\alpha}{\pi r \sin \theta}}$  ( $\alpha = 1, 2$  specifies different coefficients for different subdomains  $\Omega_\alpha$ ), and

$$\psi(w, \mathbf{r}, \mathbf{r}') = \begin{cases} ik_1 \cos(w - \theta) & \mathbf{r} \in \Omega_1 \\ ik_2 \cos(w - \theta) & \mathbf{r} \in \Omega_2 \end{cases} \quad (3.6)$$

$$\mathcal{V}(w, \mathbf{r}, \mathbf{r}') = \begin{cases} \sqrt{\sin w} e^{-ik_1 r' \sin w \sin \theta' \cos(\phi - \phi')} \left[ e^{(-ik_1 \cos w z')} + f(w) e^{(ik_1 \cos w z')} \right] & \mathbf{r} \in \Omega_1 \\ \sqrt{\sin w} e^{-ik_2 r' \sin w \sin \theta' \cos(\phi - \phi')} e^{(ik_{z_1}(w) z')} (1 + f(w)) & \mathbf{r} \in \Omega_2 \end{cases} \quad (3.7)$$

Note that  $(r, \theta, \phi)$  and  $(r', \theta', \phi')$  are the spherical coordinates of  $\mathbf{r}$  and  $\mathbf{r}'$ , respectively, where  $r = |\mathbf{r}|$ ,  $\theta$  is the longitudinal angle with respect to  $z$  and  $\phi$  is the azimuthal angle in the  $x$ - $y$  plane.

(3.5) is in a suitable form for asymptotic evaluations. In general, the asymptotic analysis of radiation integrals in complex plane consists of examining following additive contributions:

- Saddle point contribution

The stationary phase method is used to derive it [14, Ch. 4].

- Critical point contributions

There are three types of critical points:

- branch point singularity
- pole singularity
- integration end points.

The far-field asymptotics of each contribution can be determined using the method of steepest descent [14, Ch. 3] and [3, Ch. 7].

### 3.1 Saddle point contribution

To keep the procedure clear, we only discuss (3.5) in  $\Omega_1$ . Same calculations can be used for the integration in  $\Omega_2$ .

The integral in  $\Omega_1$  has only one first order saddle point at  $w_s = \theta$

$$\psi'(w_s) = 0 \text{ and } \psi''(w_s) \neq 0 \quad (3.8)$$

where  $\psi'$  and  $\psi''$  mean the first and the second derivatives of  $\psi$  with respect to  $w$ , respectively. The steepest-descent path ( $\bar{P}_s$ ) through the saddle point lies on  $\text{Im } \psi(w) = \text{const}$ , that is  $\text{Im } \psi(w) = \text{Im } \psi(w_s)$ . If the medium is loss-less, then the Steepest Descent Path (SDP) is:

$$\text{Im } \psi(w) = k_1 \cos(\text{Re } w - \theta) \cosh(\text{Im } w) = k_1 \quad (3.9)$$

The directions of the SDP at the saddle point are  $-\frac{\pi}{4}$  and  $\frac{3\pi}{4}$  [3, Sec. 7.2, table 7.1]. For this problem, integration contours must be along a direction which conserves the boundedness of the integrands when  $r \rightarrow \infty$ . The phase term in (3.5) is

$$r\psi(w) = rk_1 [\sin(\operatorname{Re} w - \theta) \sinh(\operatorname{Im} w) + i \cos(\operatorname{Re} w - \theta) \cosh(\operatorname{Im} w)]. \quad (3.10)$$

In order to have bounded integrands for observation points located away from the scatterer we must have

$$\sin(\operatorname{Re} w - \theta) \sinh(\operatorname{Im} w) < 0 \quad (3.11)$$

which means

$$\begin{cases} 0 < \operatorname{Re} w - \theta < \frac{\pi}{2} & \rightarrow \operatorname{Im} w < 0 \\ -\frac{\pi}{2} < \operatorname{Re} w - \theta < 0 & \rightarrow \operatorname{Im} w > 0 \end{cases} \quad (3.12)$$

Consequently, we choose  $\bar{P}_s$  along  $-\frac{\pi}{4}$  and keep  $\bar{P}_w$  and  $\bar{P}_s$  in those regions of  $w$  plane that (3.11) is fulfilled (see Figure 8).

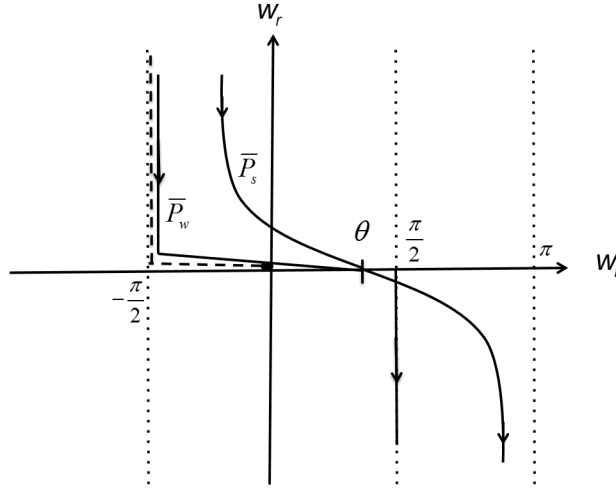


Figure 8: Integration contours in the complex  $w$  plane.  $\bar{P}_s$  is the steepest descent path (SDP).

**Theorem 3.2.** ([14, Ch. 3, Page 50]) *if  $\mathcal{V}(w, \mathbf{r}, \mathbf{r}')$  does not have any singularity at  $w = w_s$ , then the asymptotic form of the radiation integral (3.5) along SDP is*

$$\begin{aligned} g_s(\mathbf{r}, \mathbf{r}') &= C(\mathbf{r}, \mathbf{r}') \int_{\bar{P}_s} \mathcal{V}(w, \mathbf{r}, \mathbf{r}') e^{r\psi(w, \mathbf{r}, \mathbf{r}')} dw \\ &\sim C(\mathbf{r}, \mathbf{r}') \sqrt{\frac{-2\pi}{r\psi''(w_s)}} \mathcal{V}(w_s, \mathbf{r}, \mathbf{r}') e^{r\psi(w_s, \mathbf{r}, \mathbf{r}')} \end{aligned} \quad (3.13)$$

$$= \begin{cases} \frac{e^{ik_1 r}}{4\pi r} e^{-ik_1(\sin\theta \cos\phi x' + \sin\theta \sin\phi y')} \left[ e^{-ik_1 \cos\theta z'} + f(\theta) e^{ik_1 \cos\theta z'} \right] & \mathbf{r} \in \Omega_1 \\ \frac{e^{ik_2 r}}{4\pi r} e^{-ik_2(\sin\theta \cos\phi x' + \sin\theta \sin\phi y')} e^{-ik_2 \sqrt{\frac{\epsilon_1}{\epsilon_2} - \sin^2\theta} z'} (1 + f(\theta)) & \mathbf{r} \in \Omega_2 \end{cases}$$

The result obtained above is valid as far as no singularity exists in the vicinity of the saddle point. In Section 3.3, it will be shown that a pole singularity shows up near the saddle point under some special conditions. In this case, the final result for integrating along SDP changes. More details are given in Section 3.3.

### 3.2 Branch point contribution

As explained in Section 2.3, (3.5) has only one branch cut. In  $\Omega_1$ ,  $k_{z_2} = k_1 \sqrt{\eta - \sin^2 w}$  is the source of branch cut at  $\sin(w_b) = \sqrt{\eta}$ . For a special observation angle  $\theta_b$ , the branch point  $w_b$  lies on  $\bar{P}_s$ . Using (3.9), we derive  $\theta_b$  as

$$\theta_b = \operatorname{Re} w_b - \cos^{-1} \left( \frac{1}{\cosh(\operatorname{Im} w_b)} \right). \quad (3.14)$$

If  $\theta > \theta_b$  the branch point intersects with the SDP. For an intersected  $w_b$ , we surround the branch cut with an appropriate contour  $\bar{P}_b$  (see Figure 9).

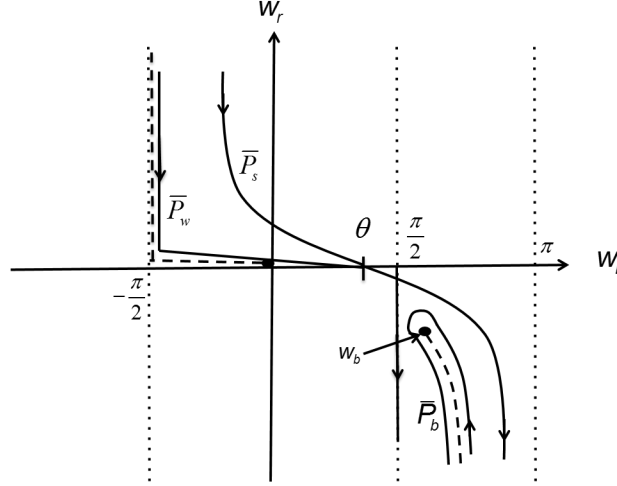


Figure 9: Integration contours in the complex  $w$  plane.  $w_b$  is the branch point and  $\bar{P}_b$  surrounds the branch cut.

**Theorem 3.3.** *The asymptotic form of the radiation integral (3.5) along the contour  $\bar{P}_b$  is [11]:*

$$g_b(\mathbf{r}, \mathbf{r}') = C(\mathbf{r}, \mathbf{r}') \int_{\bar{P}_b} \mathcal{V}(w, \mathbf{r}, \mathbf{r}') e^{r\psi(w, \mathbf{r}, \mathbf{r}')} dw$$

$$\sim C(\mathbf{r}, \mathbf{r}') \frac{\mathcal{V}_0 \sqrt{\pi}}{(r|\psi'(w_b)|)^{\frac{3}{2}}} e^{r\psi(w_b)} \quad (3.15)$$

$$(3.16)$$

where  $\mathcal{V} \sim \mathcal{V}_0 \sqrt{(w - w_b)}$ ,  $w \rightarrow w_b$ .

Using Theorem 3.3, one can derive  $g_b(\mathbf{r}, \mathbf{r}')$  for TM modes as follows

$$g_b(\mathbf{r}, \mathbf{r}') = \begin{cases} \frac{e^{-i\frac{\pi}{4}}}{4\pi} \sqrt{\frac{k_1}{r \eta \sin \theta}} e^{-ik_2(\cos \phi x' + \sin \phi y')} & \mathbf{r} \in \Omega_1 \\ \frac{\exp(ik_1(\sqrt{1-\eta}(z+z') + \sqrt{\eta}\rho))}{[k_1(\sqrt{1-\eta} r \sin \theta - \sqrt{\eta} r \cos \theta)]^{\frac{3}{2}} (1-\eta)^{\frac{1}{4}}} U(\theta - \theta_b) & \\ \frac{e^{i\frac{3\pi}{4}}}{4\pi} \sqrt{\frac{k_2}{r \eta \sin \theta}} e^{-ik_1(\cos \phi x' + \sin \phi y')} & \mathbf{r} \in \Omega_2 \\ \frac{\exp(ik_2(\sqrt{1-\eta^{-1}}z + \sqrt{\eta^{-1}}\rho))}{[k_2(\sqrt{1-\eta^{-1}} r \sin \theta + \sqrt{\eta^{-1}} r \cos \theta)]^{\frac{3}{2}} (1-\eta^{-1})^{\frac{1}{4}}} U(\theta - \theta_b) & \end{cases} \quad (3.17)$$

where  $U(x) = \begin{cases} 1 & x > 0 \\ 0 & x < 0 \end{cases}$ , and  $\eta = \frac{\epsilon_2}{\epsilon_1}$ .

### 3.3 Pole contribution

In (3.5),  $f(w)$  possesses one pole singularity which must be taken into account in the case that it intersects the SDP. For the TM mode, we have

$$f(w) = \frac{\eta \cos w - \sqrt{\eta - \sin^2 w}}{\eta \cos w + \sqrt{\eta - \sin^2 w}}. \quad (3.18)$$

Thus, the pole singularity for the radiation integral in  $\Omega_1$  lies on  $\sqrt{\eta - \sin^2 w_p} = -\eta \cos w_p$ . It can be shown that

$$\cos w_p = -\frac{1}{\sqrt{1 + \eta}} \quad (3.19)$$

and

$$\sin w_p = \sqrt{\frac{\eta}{1 + \eta}}. \quad (3.20)$$

**Remark 3.2.**  $w_p$  lies on the SDP for the special observation point  $\theta_p$  which can be derived using the same procedure as for  $\theta_b$  in Section 2.3

$$\theta_p = \operatorname{Re} w_p - \cos^{-1} \left( \frac{1}{\cosh(\operatorname{Im} w_p)} \right). \quad (3.21)$$

**Theorem 3.4.** As a result of residue theorem, the pole contribution in the radiation integral (3.5) under the condition  $w_p \neq \theta$  is

$$g_p(\mathbf{r}, \mathbf{r}') = i2\pi C(\mathbf{r}, \mathbf{r}') \operatorname{Res}_{w=w_p} (\mathcal{V}(w, \mathbf{r}, \mathbf{r}') e^{r\psi(w, \mathbf{r}, \mathbf{r}')} U(\theta - \theta_p)) \quad (3.22)$$

**Remark 3.3.** It can be shown that  $w_p$  crosses the contour only under the condition that the loss of substrate material is much bigger than that in the first domain ( $|\eta| \gg 1$  and  $\arg \eta \rightarrow \pi/2$ ), and also the observation point is located on the substrate  $\theta = \pi/2$ . Under this condition and using (3.19), the pole is located at

$$w_p = \frac{\pi}{2} + \frac{1}{\sqrt{\eta}} \quad (3.23)$$

The pole derived in (3.23) lies near the saddle point ( $w_s = \theta = \frac{\pi}{2}$ ). Therefore, (3.13) is no more the correct form of integrating along the SDP. One must consider the effect of the singularity in the vicinity of the saddle point. For this end, we introduce a more generalized form of integration along the SDP,  $g_s^*(\mathbf{r}, \mathbf{r}')$  which is different from  $g_s(\mathbf{r}, \mathbf{r}')$  when  $w_p \approx w_s$

$$g_s^*(\mathbf{r}, \mathbf{r}') = \begin{cases} g_s(\mathbf{r}, \mathbf{r}') & w_p \not\approx w_s \\ g_{sp}(\mathbf{r}, \mathbf{r}') & w_p \approx w_s \end{cases} \quad (3.24)$$

**Theorem 3.5.** ([6, Sec. 4.4]) The asymptotic form of the radiation integral (3.5) along the SDP, when a pole singularity exists in the vicinity of the saddle point ( $w_p \approx \theta$ ), is

$$g_{sp}(\mathbf{r}, \mathbf{r}') \sim C(\mathbf{r}, \mathbf{r}') e^{r\psi(w_p, \mathbf{r}, \mathbf{r}')} \left[ i2a\sqrt{\pi} e^{-rb^2} Q(ib\sqrt{r}) + \sqrt{\frac{\pi}{r}} T(0) \right] \quad (3.25)$$

and

$$a = \lim_{w \rightarrow w_p} [(w - w_p)\mathcal{V}(w, \mathbf{r}, \mathbf{r}')], \quad b = \sqrt{\psi(w_s, \mathbf{r}, \mathbf{r}') - \psi(w_p, \mathbf{r}, \mathbf{r}')}$$

$$h = \sqrt{\frac{-2}{\psi''(w_s, \mathbf{r}, \mathbf{r}')}}, \quad T(0) = h\mathcal{V}(w_s, \mathbf{r}, \mathbf{r}') + \frac{a}{b}$$

$$Q(y) = \int_y^\infty e^{-x^2} dx.$$

Under the assumptions  $\theta = \pi/2$ ,  $|\eta| \gg 1$  and  $\arg \eta = \pi/2$  (3.25) becomes

$$g_{sp}(\mathbf{r}, \mathbf{r}') \sim \begin{cases} \frac{e^{ik_1 r}}{2\pi r} e^{-ik_1(\cos \phi x' + \sin \phi y')} \\ \left( 1 + i\sqrt{\pi\zeta_1} e^{-\zeta_1} - i2\sqrt{\zeta_1} e^{-\zeta_1} \int_0^{-i\sqrt{\zeta_1}} e^{-x^2} dx \right) & \mathbf{r} \in \Omega_1 \\ \frac{e^{ik_2 r}}{2\pi r} e^{-ik_1(\cos \phi x' + \sin \phi y')} \\ \left( 1 + i\sqrt{\pi\zeta_2} e^{-\zeta_2} - i2\sqrt{\zeta_2} e^{-\zeta_2} \int_0^{-i\sqrt{\zeta_2}} e^{-x^2} dx \right) & \mathbf{r} \in \Omega_2 \end{cases} \quad (3.26)$$

where  $\zeta_\alpha = \frac{k_\alpha r}{2|\eta|}$ ,  $\alpha = 1, 2$ .

### 3.4 Integration end point contribution

Equation (3.6) in  $\Omega_1$  shows that

$$\text{Im } \psi(w, \mathbf{r}, \mathbf{r}') = \cos(\text{Re } w) \sinh(\text{Im } w) \sin(\theta) - \sin(\text{Re } w) \sinh(\text{Im } w) \cos(\theta). \quad (3.27)$$

Using (3.27) and Figure 9, one can easily see that the end points of contours  $\bar{P}$ ,  $\bar{P}_s$ , and  $\bar{P}_b$  at  $|w| \rightarrow \infty$  are situated in regions wherein  $e^{ik_1 \psi(w, \mathbf{r}, \mathbf{r}')} \rightarrow 0$ . In other words no contributions arise from the end points. The same procedure applies for the integration in  $\Omega_2$ .

### 3.5 Discussion

The final form of the scalar Green's function at far away from the dipole source in the presence of a substrate is obtained by putting together all the contributions discussed earlier

$$g_0(\mathbf{r}, \mathbf{r}') = g_s^*(\mathbf{r}, \mathbf{r}') + g_b(\mathbf{r}, \mathbf{r}'). \quad (3.28)$$

Each term on the right hand side of (3.28) decays with a different rate with respect to the distance of the observation point  $\mathbf{r}$  from  $\mathbf{r}'$ . Using (3.13) and (3.17), one can see that  $g_s(\mathbf{r}, \mathbf{r}')$  and  $g_b(\mathbf{r}, \mathbf{r}')$  decay according to  $\frac{1}{r}$  and  $\frac{1}{r^2}$ , respectively. In the case of having the pole contribution, (3.26), there is a term decreasing as  $\frac{1}{\sqrt{r}}$ .

- **Saddle point contribution**

Taking a closer look at (3.13) reveals that  $g_s(\mathbf{r}, \mathbf{r}')$  comprises direct wave and reflected wave contributions in  $\Omega_1$  and the transmitted wave in  $\Omega_2$ . The first term on the right

hand side of (3.13) in  $\Omega_1$  is the spherical wave propagating directly from the source point to the observation point. This term is identical with the field of a dipole located in free space observed at far distances. The second term on the right hand side of (3.13) in  $\Omega_1$  can be interpreted as the reflected wave from the interface which is multiplied by the reflection coefficient. Finally, the saddle point contribution in  $\Omega_2$  resembles a transmitted wave through the interface. The amplitude of the transmitted wave contains the factor  $1 + f(\theta)$  which is identical to the transmission coefficient.  $g_s(\mathbf{r}, \mathbf{r}')$  can also be obtained directly through ray optics, which means that the direct and the reflected waves are observed at points located in the same half space as the source and the transmitted wave is received inside the substrate.

- **Branch point contribution**

(3.17) reveals that  $g_b(\mathbf{r}, \mathbf{r}')$  does not have that much effect on the final Green's function for the faster decay of  $\frac{1}{r^2}$  in comparison with  $g_s(\mathbf{r}, \mathbf{r}')$ . If the material is lossy,  $g_b(\mathbf{r}, \mathbf{r}')$  also decays exponentially. However, there are some exceptions, worth being taken into account:

- medium 1 loss-less, medium 2 lossy and  $\theta \rightarrow \frac{\pi}{2}$   
 $g_s(\mathbf{r}, \mathbf{r}')$  has no exponential decay in  $\Omega_1$  whereas  $g_b(\mathbf{r}, \mathbf{r}')$  decreases in both lateral and longitudinal directions in  $\Omega_1$ . As a result,  $g_s(\mathbf{r}, \mathbf{r}')$  dominates  $g_b(\mathbf{r}, \mathbf{r}')$ .  
 In  $\Omega_2$ ,  $g_s(\mathbf{r}, \mathbf{r}')$  has exponential decay in radial direction, however,  $g_b(\mathbf{r}, \mathbf{r}')$  decreases only in  $z$  direction. This means that  $g_b(\mathbf{r}, \mathbf{r}')$  dominates  $g_s(\mathbf{r}, \mathbf{r}')$  in  $\Omega_2$  when  $\rho \gg z$  or in other words  $\theta \rightarrow \frac{\pi}{2}$ .
- medium 1 lossy, medium 2 loss-less and  $\theta \rightarrow \frac{\pi}{2}$   
 $g_s(\mathbf{r}, \mathbf{r}')$  has exponential decay in  $\Omega_1$ , while  $g_b(\mathbf{r}, \mathbf{r}')$  decays only in longitudinal direction. As a result,  $g_b(\mathbf{r}, \mathbf{r}')$  dominates  $g_s(\mathbf{r}, \mathbf{r}')$  in  $\Omega_1$  when  $\rho \gg z$  or in other words  $\theta \rightarrow \frac{\pi}{2}$ . In  $\Omega_2$ , it is only  $g_b(\mathbf{r}, \mathbf{r}')$  which suffers from exponential decay.
- $\theta \rightarrow \frac{\pi}{2}$  and  $z' \rightarrow 0$   
 In this case, the ray-optical part vanishes and lower order terms,  $O(\frac{1}{r^2})$ , in the asymptotic expansion of  $g_s(\mathbf{r}, \mathbf{r}')$  become important. Under this condition, the  $g_b(\mathbf{r}, \mathbf{r}')$  contribution is comparable to the contribution of  $g_s(\mathbf{r}, \mathbf{r}')$ .

- **Pole contribution**

When medium 2 is highly lossy and medium 1 is loss-less, there can also be the effect of pole singularity (see Section 3.3). (3.26) has different terms with different decay rates on the right hand side. The first term on the right hand side of (3.26) is the same as (3.13) when the substrate is highly lossy. The second term on the right hand side of (3.26) resembles surface-waves because it decays as  $\frac{1}{\sqrt{r}}$ . However, this term does not play any significant role in the field observed at far distances because of the fast exponential decay.

## 4 Far-field closed form

As explained in the previous section, the dominant contribution to  $g_0(\mathbf{r}, \mathbf{r}')$  at far distances when  $\theta \neq 0$ ,  $\theta \neq \frac{\pi}{2}$  arises from the saddle point contribution (3.13), which means that the Green's function decays according to  $\frac{1}{r}$  as  $r \rightarrow \infty$ . Under this condition and using (2.10), one can easily see that

$$\mathbf{G}^{\mathbf{E}}(\mathbf{r}, \mathbf{r}', \hat{\ell}) = iw\mu g_0(\mathbf{r}, \mathbf{r}') \left( \hat{\theta} + \hat{\phi} \right) + O\left(\frac{1}{r^2}\right) \quad \text{as } r \rightarrow \infty \quad (4.1)$$

where  $\hat{\theta}$  and  $\hat{\phi}$  are unit vectors in polar and azimuthal directions at the point  $\hat{\ell} = (\hat{\ell}_x, \hat{\ell}_y, \hat{\ell}_z)$ .

**Remark 4.1.** Using (4.1), one can see that electromagnetic fields at far distances have only components in polar and azimuthal directions (polar coordinates). The main conclusion based on this observation is that the energy flux in the far-field area propagates only along the radial direction.

Using (4.1), one can see that  $\nabla^{\mathbf{r}} \times \mathbf{G}^{\mathbf{E}}(\mathbf{r}, \mathbf{r}', \hat{\ell}) \sim -\nabla^{\mathbf{r}'} \times \mathbf{G}^{\mathbf{E}}(\mathbf{r}, \mathbf{r}', \hat{\ell})$  as  $r \rightarrow \infty$ . So, the far-field representation of the electric field using (3.1), (3.13), and (4.1) is given by the following

**Proposition 4.1.** The electric field observed at far distances has the following asymptotic form in direction  $\hat{\ell}$

$$\mathbf{E}(\mathbf{r}) \cdot \hat{\ell} = \frac{\exp(ik_\alpha r)}{r} \left( \mathbf{E}_\infty(\hat{\mathbf{r}}) \cdot \hat{\ell} + O\left(\frac{1}{r}\right) \right) \quad \text{as } r \rightarrow \infty \quad (4.2)$$

where  $\alpha = 1, 2$ ,  $\hat{\mathbf{r}} = \mathbf{r}/r$ , and

$$\begin{aligned} \mathbf{E}_\infty(\hat{\mathbf{r}}) \cdot \hat{\ell} &= \int_{\Gamma} (\nabla^{\mathbf{r}'} \times \mathbf{E}(\mathbf{r}')) \cdot \left( \mathbf{G}_\infty(\mathbf{r}, \mathbf{r}', \hat{\ell}) \times \hat{\mathbf{n}}(\mathbf{r}') \right) \\ &\quad - \int_{\Gamma} (\nabla^{\mathbf{r}'} \times \mathbf{G}_\infty(\mathbf{r}, \mathbf{r}', \hat{\ell})) \cdot (\mathbf{E}(\mathbf{r}') \times \hat{\mathbf{n}}(\mathbf{r}')) \, ds(\mathbf{r}') \end{aligned} \quad (4.3)$$

$$\mathbf{G}_\infty(\mathbf{r}, \mathbf{r}', \hat{\ell}) = \begin{cases} \frac{\hat{\ell}}{4\pi} e^{-ik_1(\sin\theta \cos\phi x' + \sin\theta \sin\phi y')} \left[ e^{-ik_1 \cos\theta z'} + f(\theta) e^{ik_1 \cos\theta z'} \right] & \mathbf{r} \in \Omega_1 \\ \frac{\hat{\ell}}{4\pi} e^{-ik_1(\sin\theta \cos\phi x' + \sin\theta \sin\phi y')} e^{-ik_1 \sqrt{\frac{\epsilon_2}{\epsilon_1} - \sin^2\theta} z'} (1 - f(\theta)) & \mathbf{r} \in \Omega_2 \end{cases} \quad (4.4)$$

$\mathbf{E}_\infty(\hat{\mathbf{r}})$ , which is independent of the observation distance  $r$ , is known as far-field pattern. As mentioned in Remark 4.1, the electric field at far distances, has no component in radial direction, i.e.  $\mathbf{E}_\infty(\hat{\mathbf{r}})$  has only components in  $\hat{\theta}$  and  $\hat{\phi}$  directions.

For  $\hat{\ell} = \hat{\theta}$ , (2.10) shows that  $\mathbf{G}^{\mathbf{H}}(\mathbf{r}, \mathbf{r}', \hat{\ell}) \cdot \hat{z} = 0$ , which means that only the TM wave expansion must be used. Similarly, for  $\hat{\ell} = \hat{\phi}$ ,  $\mathbf{G}^{\mathbf{E}}(\mathbf{r}, \mathbf{r}', \hat{\ell}) \cdot \hat{z} = 0$ . Then the TE wave expansion must be applied.

**Proposition 4.2.** (4.3) is valid for any lipschitz surface  $\Gamma$  around the scatterer.

*Proof.* Consider a subregion  $\Omega_f$  between two closed paths  $\Gamma_i$  and  $\Gamma_o$  around the scatterer (see Figure 10). Using vector calculus we have

$$\begin{aligned} \int_{\Omega_f} (\nabla^{\mathbf{r}'} \times \nabla^{\mathbf{r}'} \times \mathbf{E}(\mathbf{r}')) \cdot \mathbf{G}_\infty(\mathbf{r}, \mathbf{r}', \hat{\ell}) \, d\mathbf{r}' &= \\ \int_{\Omega_f} (\nabla^{\mathbf{r}'} \times \mathbf{E}(\mathbf{r}')) \cdot (\nabla^{\mathbf{r}'} \times \mathbf{G}_\infty(\mathbf{r}, \mathbf{r}', \hat{\ell})) \, d\mathbf{r}' & \\ - \int_{\partial\Omega_f} (\nabla^{\mathbf{r}'} \times \mathbf{E}(\mathbf{r}')) \cdot \left( \mathbf{G}_\infty(\mathbf{r}, \mathbf{r}', \hat{\ell}) \times \hat{\mathbf{n}}(\mathbf{r}') \right) \, ds(\mathbf{r}') & \end{aligned} \quad (4.5)$$

$$\begin{aligned}
& \int_{\Omega_f} (\nabla^{\mathbf{r}'} \times \nabla^{\mathbf{r}'} \times \mathbf{G}_\infty(\mathbf{r}, \mathbf{r}', \hat{\ell})) \cdot \mathbf{E}(\mathbf{r}') \, d\mathbf{r}' = \\
& \int_{\Omega_f} (\nabla^{\mathbf{r}'} \times \mathbf{E}(\mathbf{r}')) \cdot (\nabla^{\mathbf{r}'} \times \mathbf{G}_\infty(\mathbf{r}, \mathbf{r}', \hat{\ell})) \, d\mathbf{r}' \\
& - \int_{\partial\Omega_f} (\nabla^{\mathbf{r}'} \times \mathbf{G}_\infty(\mathbf{r}, \mathbf{r}', \hat{\ell})) \cdot (\mathbf{E}(\mathbf{r}') \times \hat{n}(\mathbf{r}')) \, ds(\mathbf{r}')
\end{aligned} \tag{4.6}$$

We also know that

$$\begin{aligned}
& \nabla^{\mathbf{r}'} \times \nabla^{\mathbf{r}'} \times \mathbf{E}(\mathbf{r}') - k_\alpha^2 \mathbf{E}(\mathbf{r}') = 0 \\
& \nabla^{\mathbf{r}'} \times \nabla^{\mathbf{r}'} \times \mathbf{G}_\infty(\mathbf{r}, \mathbf{r}', \hat{\ell}) - k_\alpha^2 \mathbf{G}_\infty(\mathbf{r}, \mathbf{r}', \hat{\ell}) = 0
\end{aligned} \tag{4.7}$$

subtracting (4.6) from (4.5) and using (4.7), we have

$$\begin{aligned}
& \int_{\partial\Omega_f} (\nabla^{\mathbf{r}'} \times \mathbf{E}(\mathbf{r}')) \cdot (\mathbf{G}_\infty(\mathbf{r}, \mathbf{r}', \hat{\ell}) \times \hat{n}(\mathbf{r}')) \\
& - \int_{\partial\Omega_f} (\nabla^{\mathbf{r}'} \times \mathbf{G}_\infty(\mathbf{r}, \mathbf{r}', \hat{\ell})) \cdot (\mathbf{E}(\mathbf{r}') \times \hat{n}(\mathbf{r}')) \, ds(\mathbf{r}') = 0
\end{aligned} \tag{4.8}$$

Since  $\partial\Omega_f = \Gamma_o \cup \Gamma_i$ , we can rewrite the identity above as follows

$$\begin{aligned}
& \int_{\Gamma_o} (\nabla^{\mathbf{r}'} \times \mathbf{E}(\mathbf{r}')) \cdot (\mathbf{G}_\infty(\mathbf{r}, \mathbf{r}', \hat{\ell}) \times \hat{n}(\mathbf{r}')) \\
& - \int_{\Gamma_o} (\nabla^{\mathbf{r}'} \times \mathbf{G}_\infty(\mathbf{r}, \mathbf{r}', \hat{\ell})) \cdot (\mathbf{E}(\mathbf{r}') \times \hat{n}(\mathbf{r}')) \, ds(\mathbf{r}') \\
& = \int_{\Gamma_i} (\nabla^{\mathbf{r}'} \times \mathbf{E}(\mathbf{r}')) \cdot (\mathbf{G}_\infty(\mathbf{r}, \mathbf{r}', \hat{\ell}) \times \hat{n}(\mathbf{r}')) \\
& - \int_{\Gamma_i} (\nabla^{\mathbf{r}'} \times \mathbf{G}_\infty(\mathbf{r}, \mathbf{r}', \hat{\ell})) \cdot (\mathbf{E}(\mathbf{r}') \times \hat{n}(\mathbf{r}')) \, ds(\mathbf{r}')
\end{aligned} \tag{4.9}$$

□

**Proposition 4.3.** *The far-field pattern representation using a volume integral is [13, Section 13.6]*

$$\begin{aligned}
\mathbf{E}_\infty(\hat{\mathbf{r}}) \cdot \hat{\ell} &= \int_{\Omega_f} (\nabla^{\mathbf{r}'} \times \mathbf{E}(\mathbf{r}')) \cdot \nabla^{\mathbf{r}'} \times (\Psi(\mathbf{r}') \mathbf{G}_\infty(\mathbf{r}, \mathbf{r}', \hat{\ell})) \\
& - \int_{\Omega_f} (\nabla^{\mathbf{r}'} \times \mathbf{G}_\infty(\mathbf{r}, \mathbf{r}', \hat{\ell})) \cdot \nabla^{\mathbf{r}'} \times (\Psi(\mathbf{r}') \mathbf{E}(\mathbf{r}')) \, d\mathbf{r}'
\end{aligned} \tag{4.10}$$

where  $\Omega_f$  is a subregion between two closed paths  $\Gamma_i$  and  $\Gamma_o$  around the scatterer (see Figure 10), and  $\Psi(\mathbf{r}') \in H^1(\Omega_f)$  is a cut-off function such that

$$\Psi(\mathbf{r}')|_{\Gamma_i} \equiv 1, \text{ and } \Psi(\mathbf{r}')|_{\Gamma_o} \equiv 0 \tag{4.11}$$

*Proof.* Considering  $\Gamma = \Gamma_i$ , one can write (4.3) in the following way

$$\begin{aligned}
\mathbf{E}_\infty(\hat{\mathbf{r}}) \cdot \hat{\ell} &= \int_{\Gamma_i} (\hat{n}(\mathbf{r}') \times \nabla^{\mathbf{r}'} \times \mathbf{E}(\mathbf{r}')) \cdot (\Psi(\mathbf{r}') \mathbf{G}_\infty(\mathbf{r}, \mathbf{r}', \hat{\ell})) \\
& - \int_{\Gamma_i} (\hat{n}(\mathbf{r}') \times \nabla^{\mathbf{r}'} \times \mathbf{G}_\infty(\mathbf{r}, \mathbf{r}', \hat{\ell})) \cdot (\Psi(\mathbf{r}') \mathbf{E}(\mathbf{r}')) \, ds(\mathbf{r}')
\end{aligned} \tag{4.12}$$

The first term on the right hand side of (4.12) can be rewritten as

$$\begin{aligned} & \int_{\Gamma_i} (\hat{n}(\mathbf{r}') \times \nabla^{\mathbf{r}'} \times \mathbf{E}(\mathbf{r}')) \cdot (\Psi(\mathbf{r}') \mathbf{G}_\infty(\mathbf{r}, \mathbf{r}', \hat{\ell})) ds(\mathbf{r}') = \\ & \int_{\Omega_f} (\nabla^{\mathbf{r}'} \times \nabla^{\mathbf{r}'} \times \mathbf{E}(\mathbf{r}')) \cdot (\Psi(\mathbf{r}') \mathbf{G}_\infty(\mathbf{r}, \mathbf{r}', \hat{\ell})) d\mathbf{r}' \\ & - \int_{\Omega_f} (\nabla^{\mathbf{r}'} \times \mathbf{E}(\mathbf{r}')) \cdot (\nabla^{\mathbf{r}'} \times (\Psi(\mathbf{r}') \mathbf{G}_\infty(\mathbf{r}, \mathbf{r}', \hat{\ell}))) d\mathbf{r}' \end{aligned} \quad (4.13)$$

In the same way the second term is

$$\begin{aligned} & \int_{\Gamma_i} (\hat{n}(\mathbf{r}') \times \nabla^{\mathbf{r}'} \times \mathbf{G}_\infty(\mathbf{r}, \mathbf{r}', \hat{\ell})) \cdot (\Psi(\mathbf{r}') \mathbf{E}(\mathbf{r}')) ds(\mathbf{r}') = \\ & \int_{\Omega_f} (\nabla^{\mathbf{r}'} \times \nabla^{\mathbf{r}'} \times \mathbf{G}_\infty(\mathbf{r}, \mathbf{r}', \hat{\ell})) \cdot (\Psi(\mathbf{r}') \mathbf{E}(\mathbf{r}')) d\mathbf{r}' \\ & - \int_{\Omega_f} (\nabla^{\mathbf{r}'} \times \mathbf{G}_\infty(\mathbf{r}, \mathbf{r}', \hat{\ell})) \cdot (\nabla^{\mathbf{r}'} \times (\Psi(\mathbf{r}') \mathbf{E}(\mathbf{r}'))) d\mathbf{r}' \end{aligned} \quad (4.14)$$

subtracting (4.14) from (4.13) and keeping in mind that  $\nabla^{\mathbf{r}'} \times \nabla^{\mathbf{r}'} \times \mathbf{E}(\mathbf{r}') - k^2 \mathbf{E}(\mathbf{r}') = 0$  and  $\nabla^{\mathbf{r}'} \times \nabla^{\mathbf{r}'} \times \mathbf{G}_\infty(\mathbf{r}, \mathbf{r}', \hat{\ell}) - k^2 \mathbf{G}_\infty(\mathbf{r}, \mathbf{r}', \hat{\ell}) = 0$  we retrieve (4.10).  $\square$

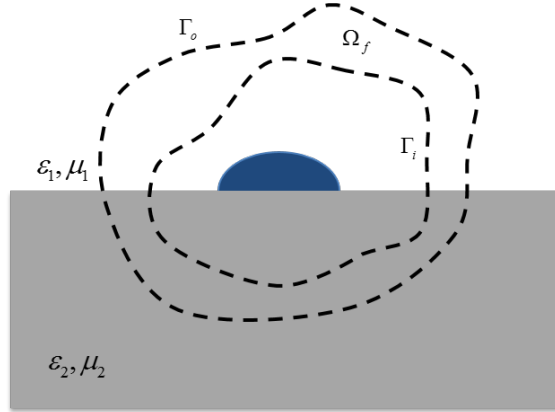


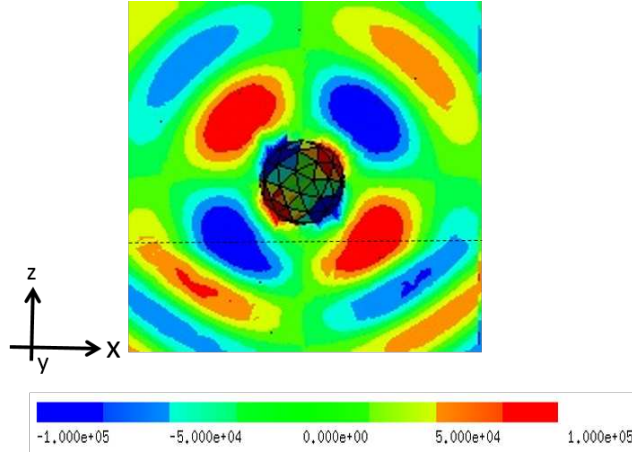
Figure 10: Volume-based far-field integration region.

## 5 Numerical results

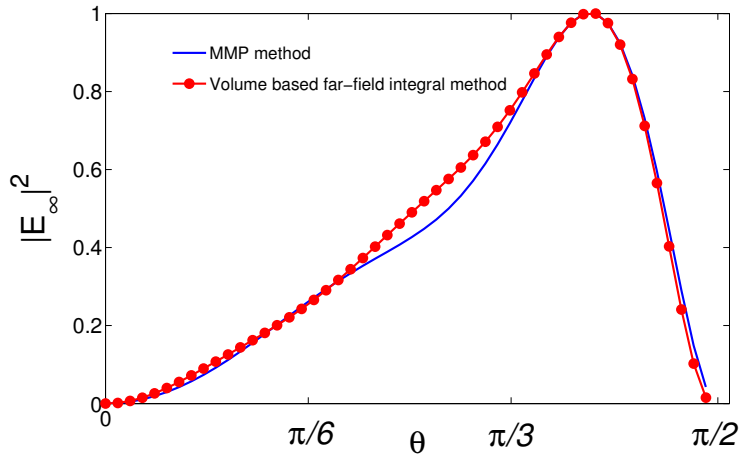
We numerically analyze the far-field pattern of different structures in the presence of a substrate. In our implementations, we use 3rd order Nedelec finite elements on a quasi-uniform tetrahedral mesh to solve Maxwell's equations in 3D structures<sup>1</sup>. The integrals in the domain are computed by a 6th order quadrature rule in each element. The unbounded computational region is truncated using a box Perfectly Matched Layer (PML). The far-field integration region  $\Omega_f$  is considered to be the domain between two spheres around the scatterer.  $r_o$  and  $r_i$  are the radius of the outer and the inner spheres, respectively. The cut-off function has the following form

$$\Psi(\mathbf{r}) = \frac{r^2 - r_o^2}{r_i^2 - r_o^2}$$

<sup>1</sup>The experiments are based on a finite element library **NGSolve** developed by Joachim Schoeberl at the University of Vienna.



(a) The finite element solution of the electric field component in the  $\hat{x}$  direction.



(b) The far-field pattern for  $\phi = 0$  and  $0 < \theta < \frac{\pi}{2}$ .

Figure 11: An electric dipole located at  $z' = 0.5\lambda$ , perpendicular to the substrate.  $\frac{\epsilon_1}{\epsilon_0} = 1$  and  $\frac{\epsilon_2}{\epsilon_0} = 2$  are the relative permittivities for  $z > 0$  and  $z < 0$ , respectively.

## 5.1 Dipole over a substrate

In the first numerical experiment, we consider an electric dipole, oriented in the direction normal to the substrate and located at the distance  $z' = 0.5\lambda$  from the substrate (see Figure 3).  $\lambda$  is the wavelength in free space. The material properties are  $(\frac{\epsilon_1}{\epsilon_0}, \frac{\mu_1}{\mu_0}) = (1, 1)$  and  $(\frac{\epsilon_2}{\epsilon_0}, \frac{\mu_2}{\mu_0}) = (2, 1)$  in domains  $z > 0$  and  $z < 0$ , respectively ( $\epsilon_0$  and  $\mu_0$  are the permittivity and permeability of free space). To avoid the singularity of the dipole field solution at the position of the dipole, we consider a sphere around the dipole and solve Maxwell's equations for the total field in the exterior region (see Figure 11a).

Figure 11b shows a close agreement between the far-field pattern calculated by (4.10) and the method of multiple multipoles (MMP) [2]. MMP is a boundary discretization method based on the field expansion using a series of basis fields. Since the far-field pattern calculation has not been implemented in MMP, we put the observation point at far distances, e.g.  $r = 1000\lambda$ , to derive the pattern. The finite element method used to solve Maxwell's equations employs 226246 degrees of freedom (DoFs). Differences between two results decrease asymptotically by refining the finite element mesh and increasing the number of expansions and matching points

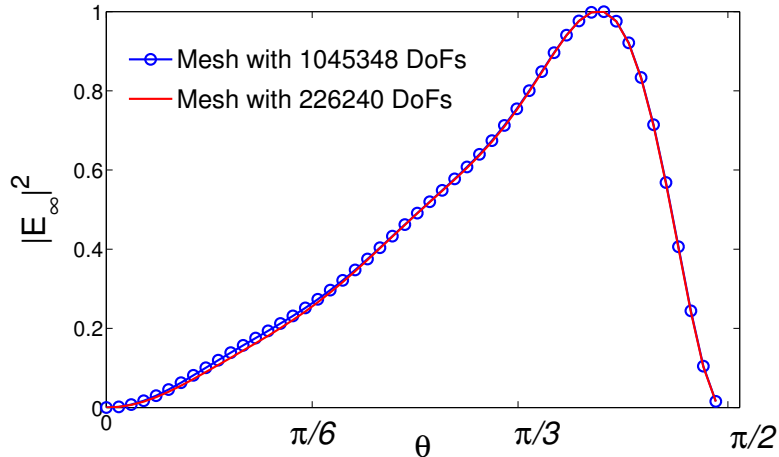


Figure 12: Comparison of the far-field pattern calculated within two different finite element meshes. The electric dipole is perpendicular to the substrate ( $\frac{\epsilon_1}{\epsilon_0} = 1$  and  $\frac{\epsilon_2}{\epsilon_0} = 2$ ).

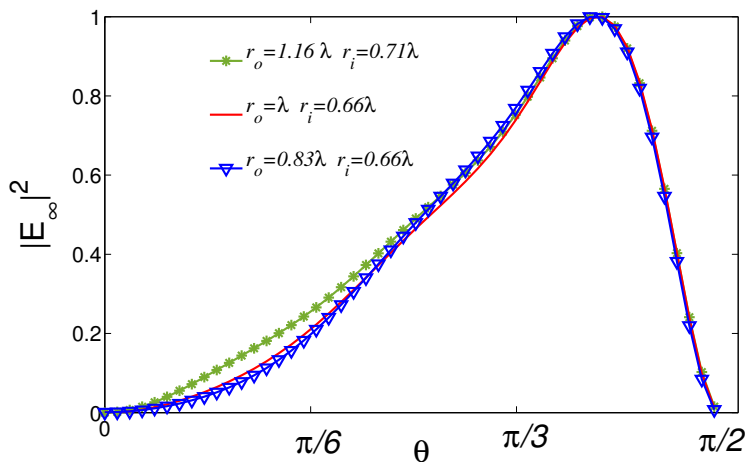
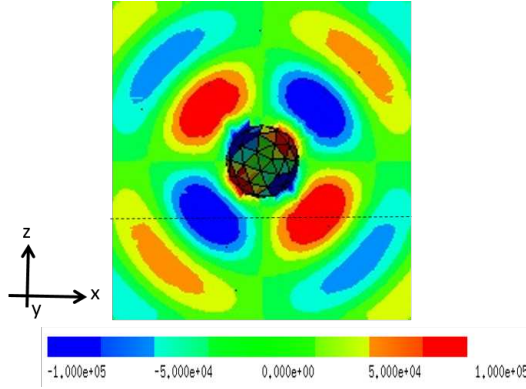


Figure 13: The far-field pattern calculated using three different integration regions. Integration domains are annuli with inner radius  $r_i$  and the outer radius  $r_o$ . The electric dipole is perpendicular to the substrate ( $\frac{\epsilon_1}{\epsilon_0} = 1$  and  $\frac{\epsilon_2}{\epsilon_0} = 2$ ), and the mesh has 226246 DoFs.

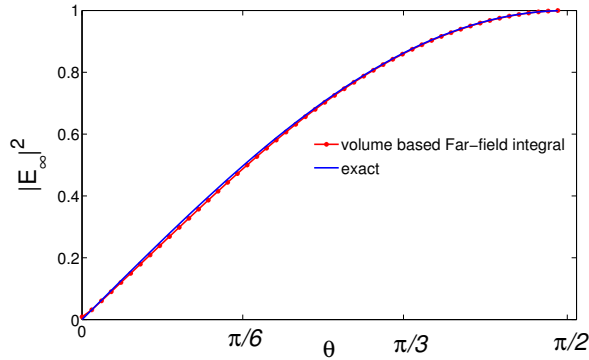
in the MMP method.

We repeat the calculations for the dipole over the substrate using a different mesh. This time we use a finer mesh with 1045348 DoFs. Based on results shown in Figure 12, the far-field pattern is almost independent of the mesh size. The volume based far-field expression is a smooth functional which averages errors over the integration region. Consequently, the local errors arising from the mesh do not have a significant effect on the final result.

Based on Proposition 4.2 the far-field pattern must be independent of the integration path. To investigate this fact, we consider three different annuli with  $(r_o, r_i) = (1.16\lambda, 0.71\lambda)$ ,  $(\lambda, 0.66\lambda)$  and  $(0.83\lambda, 0.66\lambda)$  as far-field integration regions ( $r_o$  and  $r_i$  are the outer and inner radii of the annulus, respectively) and simulate the structure using a mesh with 226246 DoFs. The results confirm our expectation and are close to each other (see Figure 13). The slight differences between results arises from the fact that we plug in the FEM solution in (4.10)



(a) The finite element solution of the electric field component in the  $\hat{x}$  direction.



(b) The far-field pattern for  $\phi = 0$  and  $0 < \theta < \frac{\pi}{2}$ .

Figure 14: An electric dipole in free-space, located at  $z' = 0.5\lambda$  and oriented in direction  $\hat{z}$ .

. When the finite element solution is employed instead of the exact solution to evaluate the far-field formula, the path independence breaks down.

For code validation, we consider the same material properties for the substrate as free space,  $(\frac{\epsilon_1}{\epsilon_0}, \frac{\mu_1}{\mu_0}) = (\frac{\epsilon_2}{\epsilon_0}, \frac{\mu_2}{\mu_0}) = (1, 1)$ . Under this assumption, we have the well-known problem of a dipole in free-space (see Figure 14a). For a dipole in free-space there exists an analytic solution  $\mathbf{E}_\infty(\hat{\mathbf{r}}) = -\frac{i\omega\mu}{4\pi} \sin\theta \hat{\theta}$  (see [8, Page 447]). Figure 14b compares the far-field pattern of a dipole in free-space derived by (4.10) with the analytic solution for  $\phi = 0$  and  $0 < \theta < \frac{\pi}{2}$ .

## 5.2 Nano-particle over a substrate

In this section, we analyze plasmon resonances of gold nanoparticles in the presence of a glass substrate (see Figure 15a). [7] had measured the scattering spectra of several cylindrical gold NPs (nanoparticles). In the first part of this section, we try to reproduce the results discussed in [7, Section 3.2]. The nanoparticle is an elliptical gold cylinder. The three principal axes of the cylinder are  $a$ ,  $b$ , and  $h$  (see Figure 15b).

As shown in [7, Section 3.1], the dipolar resonance of the structure depends on the direction of the excitation. To investigate this phenomenon, we illuminate the structure with an incident electric field parallel to one of the in-plane axes ( $a$ -axis or  $b$ -axis).

As mentioned earlier, the NP and the substrate are made of gold and glass, respectively. The refractive index of glass is  $n_2 \approx 1.5$ . However, gold is a dispersive material within the spectrum of visible light. There have been several measurements to derive the optical constants of gold [12, 17]. In this report, we use the data given in [12].

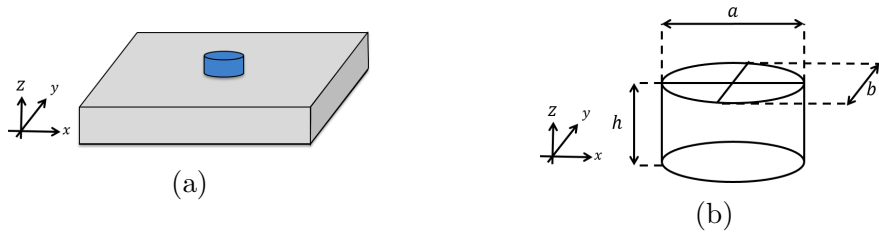


Figure 15: (a) Cylindrical nanoparticle mounted on a glass substrate with (b) 3 principal axes  $a$ ,  $b$ , and  $h$ .

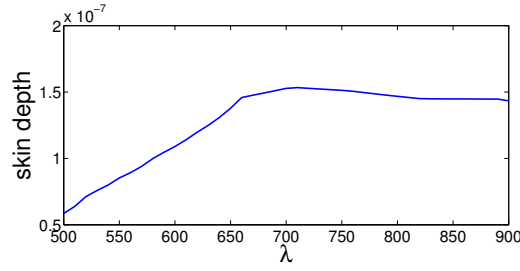


Figure 16: Skin depth of gold.

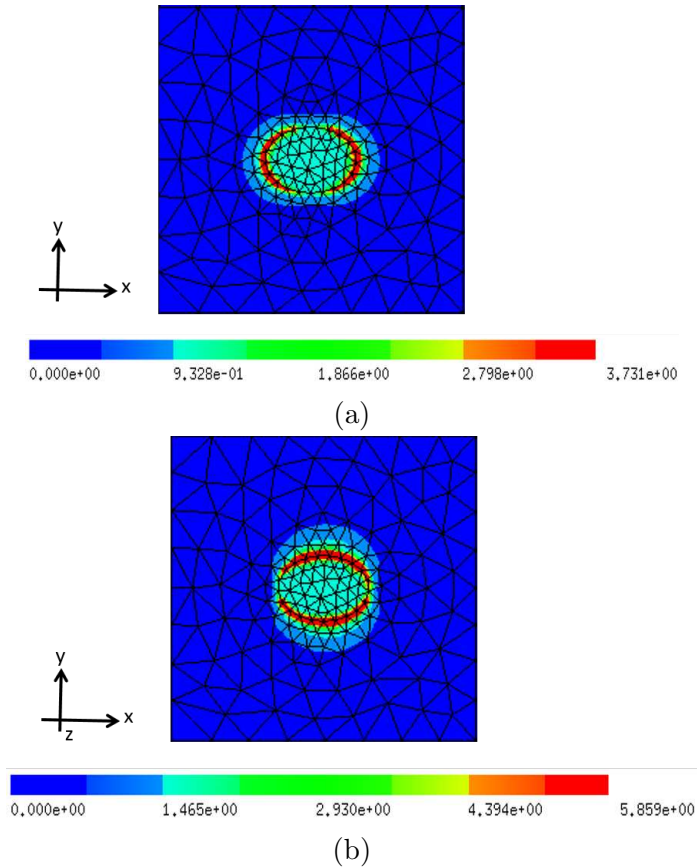


Figure 17: The absolute value of the scattered field of a cylindrical NP with elliptical footprint  $(a, b, h) = (132, 95, 110)nm$ . The incident electric field is parallel to (a) a-axis (b) b-axis.

In [7] the field is collected through an objective with the opening angle of  $\alpha = 74^\circ$  and centered on the  $z$ -axis. In order to come close to this experiment we consider the following integration

as the far-field measurement

$$Q(\lambda) = \int_{\Omega_{lens}} |\mathbf{E}_{\infty}(\mathbf{r}, \lambda)|^2 d\mathbf{r} \quad (r \rightarrow \infty). \quad (5.1)$$

where  $\Omega_{lens}$  is the area of the objective,  $\lambda$  is the wavelength in free space and  $Q(\lambda)$  is the the energy flux through the lens. To determine the mesh size, we keep in mind that gold is a lossy material, and the electromagnetic field decays rapidly inside it. There is a measure called skin depth to show how deep the electromagnetic field can penetrate inside the conductor [5, Section 5.14]. The mesh size must be small enough to model the wave attenuation within the skin depth. The smallest skin depth of gold in the range of  $\lambda = [500 : 900] \text{ nm}$  is  $59 \text{ nm}$  (see Figure 16). So, we choose the biggest mesh size  $\Delta h \approx 50 \text{ nm}$  in our simulations (see Figure 19).

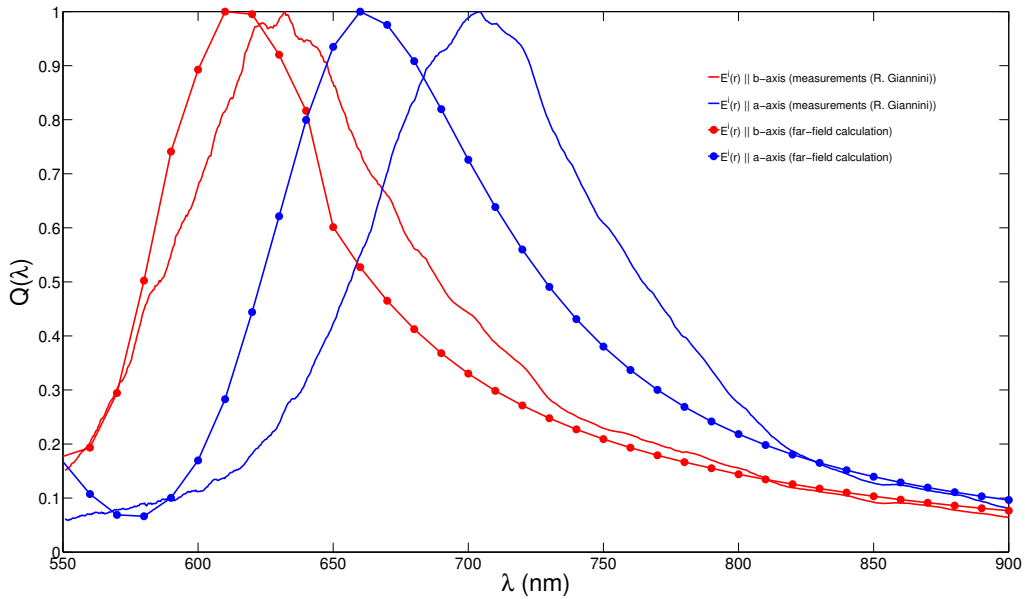
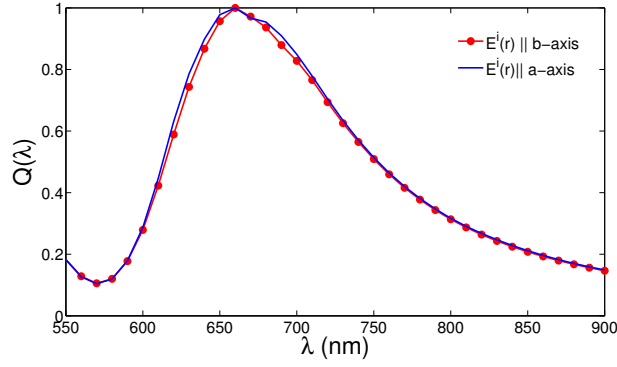


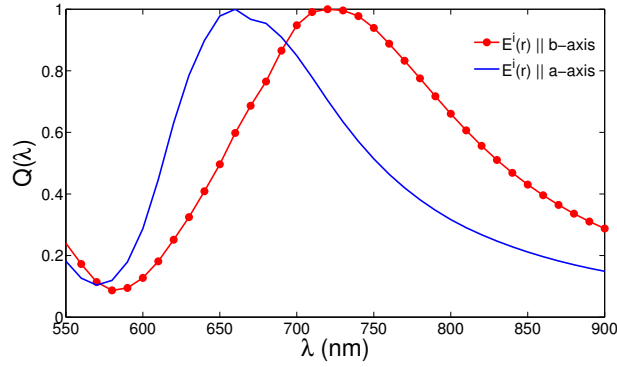
Figure 18: Normalized energy flux of a cylindrical NP with an elliptical footprint  $(a, b, h) = (132, 95, 110) \text{ nm}$ . The incident electric field  $\mathbf{E}^i(\mathbf{r})$  is either parallel to the  $a$ -axis or  $b$ -axis. The measurement results are obtained from [7, Figure 3.1].

Figure 18 shows the normalized  $Q(\lambda)$  of a cylindrical NP with elliptical footprint,  $(a, b, h) = (132, 95, 110) \text{ nm}$ . The Figure compares the results calculated by (4.10) with measurement results reported in [7, Figure 3.1]. Both measurements and calculations show the resonance-frequency shift by changing the direction of the incident electric field. Based on calculations,  $\lambda_a = 660 \text{ nm}$  and  $\lambda_b = 610 \text{ nm}$  correspond to plasmon resonance frequencies when the incident electric field is parallel to  $a$ -axis or  $b$ -axis, respectively. As it is shown in Figure 18, shapes of resonance curves are the same between measurements and simulation results. However, there is a frequency difference between them. The disagreement between measurements and simulations can be due to different problems. Some of these problems are as follows

- The shape inaccuracy of fabricated NPs.  
Shape uncertainty is inevitable During the fabrication procedure. This causes changes in the size of NPs which has a direct effect on the resonance frequency.
- Material properties of gold.  
Material properties of gold are dependent on the sample preparation procedure. The data



(a)



(b)

Figure 19: Normalized energy flux of a cylindrical NP with an elliptical footprint (a)  $(a, b, h) = (132, 132, 110) \text{ nm}$  and (b)  $(a, b, h) = (132, 160, 110) \text{ nm}$ . The incident electric field  $\mathbf{E}^i(\mathbf{r})$  is either parallel to the  $a$ -axis or  $b$ -axis.

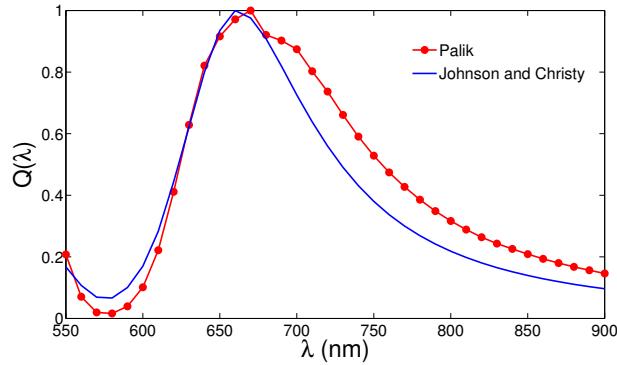


Figure 20: Normalized energy flux of a cylindrical NP with elliptical footprint  $(a, b, h) = (132, 95, 110) \text{ nm}$  calculated using different databases for optical constants of gold.

given by [12, 17] are based on measurements on bulk gold material which is not adequate in our experiments.

- The size and the location of the objective.

To see the effect of axis size on the resonance frequency, we change the size of  $b$ -axis to  $132 \text{ nm}$  and  $160 \text{ nm}$  while the sizes of  $a$  and  $h$  axes are fixed.  $\lambda_b$  shifts to the right by increasing the axis size, whereas  $\lambda_a$  remains almost constant (see Figures 19a and 19b). Based on this experiment, any changes in the the shape of NP has a direct effect on the resonance frequency.

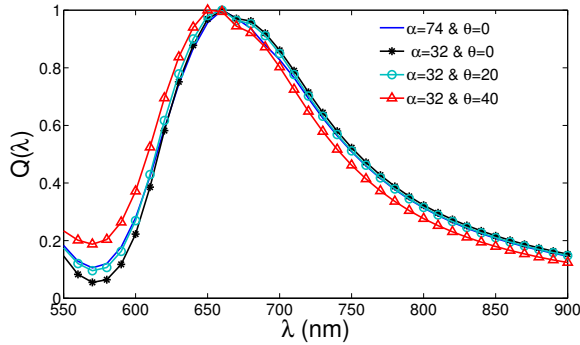


Figure 21: Normalized energy flux of a cylindrical NP with circular footprint  $(a, b, h) = (132, 132, 110)$  nm calculated by lenses with different opening angle ( $\alpha$ ) and centered at different angles with respect to the  $z$ -axis ( $\beta$ ).

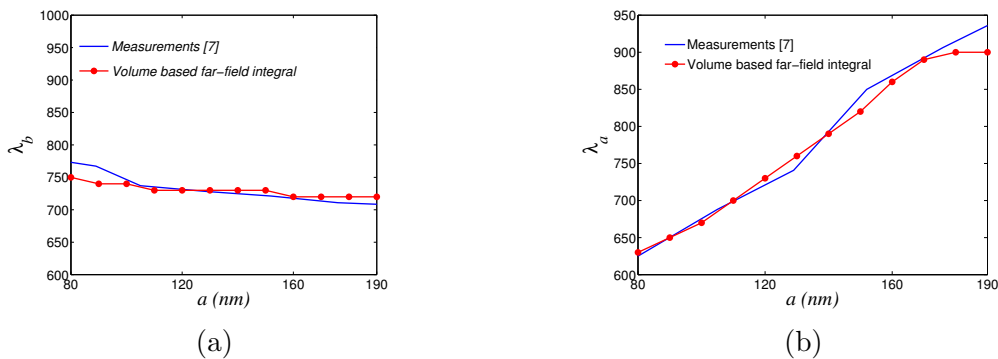


Figure 22: Dependence of the resonance frequency on the size of principal axis. The footprint is elliptical and  $(a, b, h) = (80 : 190, 120, 20)$  nm. The incident electric field is parallel to (a)  $b$ -axis and (b)  $a$ -axis. The measurement results are from [7, Figure 6.1].

To see how sensitive  $Q(\lambda)$  is to the gold characteristics, we repeat the calculations for the elliptical footprint  $(a, b, h) = (132, 95, 110)$  nm using the data given by Palik [17] and compare them with the results based on Johnson and Christy data [12]. As one can see, the resonance frequency is not affected significantly by the changes in gold constants obtained from different measurements, but the shape of the resonance curve changes significantly (see Figure 20). From the curve obtained using Palik's data, one even might think that a second resonance is present near  $700$  nm. But this is only because of material properties.

The effect of the size and the position of the objective on the normalized energy flux is investigated using lenses centered at different angles with respect to the  $z$ -axis  $\beta$ , and with different opening angles  $\alpha$ . The results show that  $Q(\lambda)$  is almost independent of objective lens parameters (see Figure 21).

Based on the discussion above, the shape inaccuracy of fabricated NPs plays the most significant role in making differences between simulation and measurement results. The size effect has been studied even more closely in [7, Figure 6.1]. It shows how the resonance frequency of different cylindrical NPs depends on the size of the in-plane axis. The  $b$ -axis is kept constant and the  $a$ -axis changes  $80 < a < 190$  nm. We repeat the same experiment with the elliptical foot print,  $b = 120$  nm and  $h = 20$  nm and compare them with measurements (see Figure 22). As one can see, a good agreement between simulations and measurements

is observed.  $\lambda_b$  reduces rapidly for the small values of in-plane axial ratio ( $\frac{a}{b} < 1$ ), but it remains almost constant for axial ratios bigger than 1 (See Figure 22a). However,  $\lambda_a$  increases by increasing the  $a$ -axis size (see Figure 22b).

## 6 Conclusion

Near-field to far-field mapping is a technique to indirectly evaluate the values of electromagnetic fields at far distances. For objects located in free space there is a closed formulation. The procedure gets more challenging for layered media and had remained unsolved for a long time. We presented rigorous asymptotics for the Green's function in semi-infinite half space, and a closed form far-field mapping technique is derived. The mapping can be expressed either as an integration in volume or as an integration on boundary. It is advisable to use the volume integration when the finite element method is used. Numerical experiments also show a very good agreement with other methods.

## References

- [1] Ablowitz, M.J., Fokas, A.S.: Complex variables: Introduction and applications. Cambridge text in applied mathematics. Cambridge university press, Cambridge, UK, 2nd edition. (2003)
- [2] Alparslan, A., Hafner, C.: Layered geometry green's functions in the multiple multipole program. *J. Comput. Theor. Nanosci.* **8**(8), 1600–8 (2011)
- [3] Bleistein, N.: Mathematical methods for wave phenomena. Academic Press, Orlando, USA. (1984)
- [4] Chew, W.C.: Waves and fields in inhomogeneous media. Van Nostrand Reinhold. (1990)
- [5] Edward Conrad Jordan, K.G.B.: Electromagnetic Waves and Radiating Systems. Prentice-Hall. (1968)
- [6] Felsen, L.B.: Radiation and scattering of waves. Prentice-Hall, Inc., Englewood Cliffs, New Jersey. (1973)
- [7] Giannini, R.: Shape dependence of LSPRs and their applications in nanoemitters. PhD. thesis, ETH University of Zurich. (2014)
- [8] Griffiths, D.J.: Introduction to electrodynamics. Prentice Hall (1999)
- [9] v Hoerschelmann, H.: Ueber die wirkungsweise des geknickten marconischen senders in der drahtlosen telegraphie. *Jb. drahtl. Telegr. u. Teleph.* **5**, 14–34 (1911)
- [10] I. R. Capoglu A. Taflove, V.B.: A frequency-domain near-field-to-far-field transform for planar layered media. *IEEE Trans. Antennas Propag* **60**(4), 1878–85 (2012)
- [11] J.Hanckes, C., Nedelec, J.C.: Asymptotics for helmholtz and maxwell solutions in 3d open waveguides. *Commun. Comput. Phys.* **11**(2), 629–46 (2012)
- [12] Johnson, P.B., Christy, R.W.: Optical constants of the noble materials. *Phys. Rev. B.* **6**(12), 4370–9 (1972)
- [13] Monk, P.: Finite element methods for Maxwell's equations. Oxford University Press (2003)
- [14] Murray, J.D.: Asymptotic analysis. Springer Verlag, INC., New York, USA. (1984)
- [15] Nedelec, J.C.: Acoustic and electromagnetic equations. Springer-Verlag New Yourk, Inc. (2001)
- [16] Novotny, L.: Principles of nano optics. Cambridge University Press. (2006)
- [17] Palik, E.D.: Handbook of optical constants of solids. Academic Press, Boston. (1985)
- [18] van der Pol, B., Niessen, K.F.: Ueber die ausbreitung elektromagnetischer wellen ueber einer ebenen erde. *Ann. Physik* **6**, 273–294 (1930)
- [19] Sommerfeld, A.: Ueber die ausbreitung der wellen in der drahtlosen telegraphie. *Ann. Physik* **28**, 665–736 (1909)
- [20] Sommerfeld, A.: Partial differential equations in physics. New York: Academic Press. (1964)

- [21] Weyl, H.: Ausbreitung elektromagnetischer wellen ueber einem ebenen leiter. Ann. Physik **60**, 481–500 (1919)
- [22] Zenneck, J.: Fortpflanzung ebener elektromagnetischer wellen laengs einer ebenen leiterflaeche. Ann. Physik **23**, 848–866 (1907)

## Recent Research Reports

Nr.	Authors/Title
2014-32	R. Casagrande and C. Winkelmann and R. Hiptmair and J. Ostrowski DG Treatment of Non-Conforming Interfaces in 3D Curl-Curl Problems
2014-33	U. Fjordholm and R. Kappeli and S. Mishra and E. Tadmor Construction of approximate entropy measure valued solutions for systems of conservation laws.
2014-34	S. Lanthaler and S. Mishra Computation of measure valued solutions for the incompressible Euler equations.
2014-35	P. Grohs and A. Obermeier Ridgelet Methods for Linear Transport Equations
2014-36	P. Chen and Ch. Schwab Sparse-Grid, Reduced-Basis Bayesian Inversion
2014-37	R. Kaeppli and S. Mishra Well-balanced schemes for gravitationally stratified media
2014-38	D. Schoetzau and Ch. Schwab Exponential Convergence for hp-Version and Spectral Finite Element Methods for Elliptic Problems in Polyhedra
2014-39	P. Grohs and M. Sprecher Total Variation Regularization by Iteratively Reweighted Least Squares on Hadamard Spaces and the Sphere
2014-40	R. Casagrande and R. Hiptmair An A Priori Error Estimate for Interior Penalty Discretizations of the Curl-Curl Operator on Non-Conforming Meshes
2015-01	X. Claeys and R. Hiptmair Integral Equations for Electromagnetic Scattering at Multi-Screens